Is every strong lens model unhappy in its own way? Uniform modelling of a sample of 13 quadruply+ imaged quasars

A. J. Shajib [1]*, S. Birrer,[1] T. Treu,[1]† M. W. Auger,[2] A. Agnello,[3] T. Anguita [4,5] E. J. Buckley-Geer,[6] J. H. H. Chan,[7] T. E. Collett [8] F. Courbin,[7] C. D. Fassnacht,[9] J. Frieman,[6,10] I. Kayo,[11] C. Lemon [2] H. Lin,[6] P. J. Marshall,[12] R. McMahon,[2] A. More [13] N. D. Morgan,[14] V. Motta,[15] M. Oguri,[16,17,18] F. Ostrovski,[2] C. E. Rusu [19]‡ P. L. Schechter,[20] T. Shanks [21] S. H. Suyu,[22,23,24] G. Meylan,[7] T. M. C. Abbott,[25] S. Allam,[6] J. Annis,[6] S. Avila,[8] E. Bertin,[26,27] D. Brooks,[28] A. Carnero Rosell,[29,30] M. Carrasco Kind,[31,32] J. Carretero,[33] C. E. Cunha,[34] L. N. da Costa,[29,30] J. De Vicente,[35] S. Desai,[36] P. Doel,[28] B. Flaugher,[6] P. Fosalba,[37,38] J. García-Bellido,[39] D. W. Gerdes,[40,41] D. Gruen,[34,42] R. A. Gruendl,[31,32] G. Gutierrez,[6] W. G. Hartley,[28,43] D. L. Hollowood,[44] B. Hoyle,[45,46] D. J. James,[47] K. Kuehn,[48] N. Kuropatkin,[6] O. Lahav,[28] M. Lima,[29,49] M. A. G. Maia,[29,30] M. March,[50] J. L. Marshall,[51] P. Melchior,[52] F. Menanteau,[31,32] R. Miquel,[53] A. A. Plazas,[54] E. Sanchez,[35] V. Scarpine,[6] I. Sevilla-Noarbe,[35] M. Smith,[55] M. Soares-Santos,[56] F. Sobreira,[28,57] E. Suchyta,[58] M. E. C. Swanson,[32] G. Tarle[41] and A. R. Walker[25]

Affiliations are listed at the end of the paper

ABSTRACT

Strong-gravitational lens systems with quadruply imaged quasars (quads) are unique probes to address several fundamental problems in cosmology and astrophysics. Although they are intrinsically very rare, ongoing and planned wide-field deep-sky surveys are set to discover thousands of such systems in the next decade. It is thus paramount to devise a general framework to model strong-lens systems to cope with this large influx without being limited by expert investigator time. We propose such a general modelling framework (implemented with the publicly available software LENSTRONOMY) and apply it to uniformly model three-band *Hubble Space Telescope* Wide Field Camera 3 images of 13 quads. This is the largest uniformly modelled sample of quads to date and paves the way for a variety of studies. To illustrate the scientific content of the sample, we investigate the alignment between the mass and light distribution in the deflectors. The position angles of these distributions are well-aligned, except when there is strong external shear. However, we find no correlation between the ellipticity of the light and mass distributions. We also show that the observed flux-ratios between the images depart significantly from the predictions of simple smooth models. The departures are strongest in the bluest band, consistent with microlensing being the dominant cause in addition to millilensing. Future papers will exploit this rich data set in combination with ground-based spectroscopy and time delays to determine quantities such as the Hubble constant, the free streaming length of dark matter, and the normalization of the initial stellar mass function.

* E-mail: ajshajib@astro.ucla.edu
† Packard Fellow.
‡ Subaru Fellow.

1 INTRODUCTION

Strong gravitational lensing is the effect where light from a background object is deflected by a foreground mass distribution (e.g. galaxy or galaxy cluster) and multiple images of the background object form. Strong gravitational lenses are powerful probes to answer a variety of astrophysical and cosmological questions (see e.g. Treu 2010), as we discuss briefly below.

According to the concordance model in cosmology, our Universe consists of 5 per cent baryonic matter, 26 per cent dark matter, and 69 per cent dark energy accounting for a cosmological constant Λ (Planck Collaboration VI 2018). This model is known as the Λ cold dark matter (ΛCDM) model. The predictions of the ΛCDM model have been extensively tested with good agreement to observations spanning from the largest scale up to the horizon down to ~ 1 Mpc (e.g. Dawson et al. 2013; Shajib & Wright 2016; Planck Collaboration VI 2018). However, there also have been observations that are in tension with the flat ΛCDM paradigm. For instance, there is a tension at the $\gtrsim 3\sigma$ level between the local measurement of H_0 from Type Ia supernovae (Bernal, Verde & Riess 2016; Riess et al. 2016, 2018a, 2018b) and that extrapolated from the *Planck* cosmic microwave background measurement for a flat ΛCDM cosmology. This tension may arise from unknown systematic uncertainties in one or both of the measurements, or might point to new physics, e.g. additional species of relativistic particles, a non-flat cosmology, or dynamic dark energy. Therefore, it is crucial to have precise and independent measurements of H_0 to settle this discrepancy.

In a gravitational lens, if the background source is time-variable (typically a quasar, but also a supernova as originally proposed), the delay between the arrival time of photons for the different images can be used to measure the so-called time-delay distance (Refsdal 1964; Suyu et al. 2010). This distance is inversely proportional to H_0, thus it can be used to constrain H_0 and other cosmological parameters (for a detailed review, see Treu & Marshall 2016). H_0 has been determined to 3.8 per cent precision using three lens systems in the flat ΛCDM cosmology (Suyu et al. 2010, 2013, 2017; Bonvin et al. 2017; Rusu et al. 2017; Sluse et al. 2017; Wong et al. 2017; Tihhonova et al. 2018). With a large sample size of about 40 lenses, it is possible to measure H_0 with the per cent precision (Jee et al. 2016; Shajib, Treu & Agnello 2018) necessary to resolve the H_0 tension and make the most of other dark energy probes (Linder 2011; Suyu et al. 2012; Weinberg et al. 2013).

One of the baryonic components in dark matter is low-mass star. Surprisingly, recent studies have shown that the low-mass star contribution in massive elliptical galaxies is significantly underestimated if the stellar initial mass function (IMF) of the Milky Way is assumed (Treu et al. 2010; van Dokkum & Conroy 2010; Auger et al. 2010a; Cappellari et al. 2012; Schechter et al. 2014). Precise knowledge about the IMF is key in measuring almost any extragalactic quantity involving star and metal formation. Measuring the stellar mass-to-light ratio in the deflectors of quadruply imaged lensed quasars (henceforth quads) from microlensing statistics provides one of the most robust methods to constrain the IMF (e.g. Oguri, Rusu & Falco 2014; Schechter et al. 2014).

Quads also provide a unique test of small-scale structure formation (Kauffmann, White & Guiderdoni 1993; Witt, Mao & Schechter 1995; Klypin et al. 1999; Moore et al. 1999; Metcalf & Madau 2001; Dalal & Kochanek 2002; Yoo et al. 2006; Keeton & Moustakas 2009; Moustakas et al. 2009; Boylan-Kolchin, Bullock & Kaplinghat 2011) by measuring the subhalo mass function (Metcalf & Zhao 2002; Kochanek & Dalal 2004; Amara et al. 2006; Metcalf & Amara 2012; Nierenberg et al. 2014, 2017; Xu et al. 2015; Birrer, Amara & Refregier 2017, see also for studies involving extended source only, Koopmans 2005; Vegetti & Koopmans 2009; Vegetti et al. 2010, 2012, 2018; Hezaveh et al. 2016), independent of their luminosity function. With a large sample of quads, Gilman et al. (2018) demonstrate the possibility of constraining the free-streaming length of dark matter particles more precisely than current limits based on the Ly α forest (Viel et al. 2013).

Until recently, all of these methods could only be applied to a small sample of known quads. However, such systems are currently being discovered at a rapidly increasing rate due to multiple strong-lens search efforts involving various large-area sky surveys (e.g. Agnello et al. 2015, 2018b,c; Williams, Agnello & Treu 2017; Schechter et al. 2017; Anguita et al. 2018; Lemon et al. 2018; Sonnenfeld et al. 2018; Treu et al. 2018; Williams et al. 2018). With more deep wide-field surveys, e.g. *Wide-Field Infrared Survey Telescope*, Large Synoptic Survey Telescope, and *Euclid*, coming online within the next decade, the sample size of quads is expected to increase by two orders of magnitude or more (Oguri & Marshall 2010; Collett 2015).

Modelling such lens systems has so far been carried out for individual systems while fine-tuning the modelling approach on a case-by-case basis. However, with the rapidly increasing rate of discovery, it is essential to develop a modelling technique that is applicable to a wide variety of quads to efficiently reduce the time and human labour necessary in this endeavour. Given the large diversity in the morphology and complexity of quads, this is an interesting problem to pose: is every quad different or 'unhappy in its own way' that requires careful decision-making by a human in the modelling procedure, or are the quads similar or 'happy' to some extent so that a uniform modelling technique can be applied to generate acceptable models without much human intervention?

Recently, some initial strides have been undertaken along the lines of solving this problem for strong lenses with extended sources. Nightingale, Dye & Massey (2018) devised an automated lens modelling procedure using Bayesian model comparison. Hezaveh, Levasseur & Marshall (2017) and Perreault Levasseur, Hezaveh & Wechsler (2017) applied machine learning techniques to automatically model strong gravitational lenses and constrain the model parameters. In this paper, we devise a general framework or decision tree that can be applied to model-fitting of quads both in a single band and simultaneously in multiple bands. We implement this uniform modelling approach using the publicly available lens-modelling software LENSTRONOMY (Birrer & Amara 2018, based on Birrer, Amara & Refregier 2015) to a sample of 13 quads from the *Hubble Space Telescope* (*HST*) data in three bands. LENSTRONOMY comes with sufficient modelling tools and the architecture allows a build-up in complexity as presented in this work. We report the model parameters and other derived quantities for these lens systems.

To demonstrate the scientific capabilities of such a sample of strong-lens systems, we study the properties of the deflector galaxy mass distribution, specifically the alignment of the mass and light

distributions in them. The distribution of dark matter and baryons in galaxies can test predictions of ΛCDM and galaxy formation theories (e.g. Dubinski 1994; Ibata et al. 2001; Kazantzidis et al. 2004; Macciò et al. 2007; Debattista et al. 2008; Lux et al. 2012; Read 2014). *N*-body simulations with only dark matter particles predict nearly triaxial, prolate haloes (Dubinski & Carlberg 1991; Warren et al. 1992; Navarro, Frenk & White 1996; Jing & Suto 2002; Macciò et al. 2007). In the presence of baryons, the haloes become rounder (Dubinski & Carlberg 1991; Warren et al. 1992; Dubinski 1994). With a modestly triaxial luminous galaxy embedded in the dark matter halo, large misalignments ($\sim 16 \pm 19°$) between the projected light and mass major axes can be produced (Romanowsky & Kochanek 1998). For disc galaxies, the dark matter distribution is shown to be well-aligned with the light distribution (Dubinski & Carlberg 1991; Katz & Gunn 1991; Debattista et al. 2008).

As the lensing effect is generated by mass, strong gravitational lenses give independent estimates of the mass distribution that can be compared with the observed light distribution. The deflectors in quads are typically massive ellipticals (with Einstein mass $M_{\rm E} \gtrsim 10^{11.5} \rm M_{\odot}$). Most of the massive ellipticals are observed to be slow rotators with uniformly distributed misalignments between the kinematic and photometric axes (Ene et al. 2018). The uniform distribution of misalignments suggests these massive ellipticals to be intrinsically triaxial. Massive ellipticals can also have of stellar populations and dust distribution with different geometries producing isophotal twist that can create a misalignment between the mass and light distributions (Goullaud et al. 2018). For lens systems, a tight alignment within $\pm 10°$ between the major axes of the mass and light distribution has been observed for deflector galaxies with weak external shear, whereas galaxies with strong external shear can be highly misaligned (Keeton, Kochanek & Falco 1998; Kochanek 2002; Treu et al. 2009; Gavazzi et al. 2012; Sluse et al. 2012; Bruderer et al. 2016). However, there has been some conflict about the correlation between the ellipticity of the mass and light distributions with reports of both strong correlation (Sluse et al. 2012; Gavazzi et al. 2012) and no correlation (Keeton et al. 1998; Ferreras, Saha & Burles 2008; Rusu et al. 2016).

This paper is organized as follows. In Section 2, we describe the data used in this study. We describe our methodology in Section 3.3 and the results in Section 4. Finally, we summarize the paper followed by a discussion in Section 5. When necessary, we adopt a fiducial cosmology with $H_0 = 70 \rm \, km \, s^{-1} \, Mpc^{-1}$, $\Omega_{\rm m} = 0.3$, $\Omega_{\Lambda} = 0.7$, and $\Omega_{\rm r} = 0$. All magnitudes are given in the AB system.

2 *HST* SAMPLE

Our sample consists of 12 quads and one five-image system. Some of these systems were discovered by the STRong-lensing Insights into the Dark Energy Survey (STRIDES)[1] collaboration [STRIDES paper I Treu et al. (2018), paper II Anguita et al. (2018), and paper III Ostrovski et al. (in preparation)], some are recent discoveries by independent searches outside of the Dark Energy Survey (DES), and some are selected from the literature. In this section, we first describe the high-resolution imaging data obtained through *HST*. We then briefly describe the lens systems in the sample.

2.1 Data

Images of the lenses were obtained using the *HST* Wide Field Camera 3 (WFC3) in three filters: F160W in the infrared (IR) channel, and F814W and F475X in the ultraviolet-visual (UVIS) channel (ID 15320, PI Treu). In the IR channel filter, we used a four-point dither pattern and STEP100 readout sequence for the MULTIACCUM mode. This approach guarantees a sufficient dynamic range to expose both the bright lensed quasar images and the extended host galaxy. For the UVIS channel filters, we used a two-point dither pattern. Two exposures at each position, one short and one long, were taken. Total exposure times for all the quads and the corresponding dates of observation are tabulated in Table 1. The data were reduced using ASTRODRIZZLE. The pixel size after drizzling is 0.08 arcsec in the F160W band, and 0.04 arcsec in the F814W and F475X bands.

2.2 Quads in the sample

In this subsection, we give a brief description of each quad in our sample (Fig. 1).

2.2.1 PS J0147+4630

This quad was serendipitously discovered from the Panoramic Survey Telescope and Rapid Response System (Pan-STARRS) survey (Berghea et al. 2017). The source redshift is $z_{\rm s} = 2.341 \pm 0.001$ (Lee 2017) and the deflector redshift is $z_{\rm d} = 0.5716 \pm 0.0004$ (Lee 2018). Initial models from the Pan-STARRS data suggest a relatively large external shear $\gamma_{\rm ext} \sim 0.13$.

2.2.2 SDSS J0248+1913

This lens system was discovered in Sloan Digital Sky Survey (SDSS) imaging data using the morphology-independent Gaussian-mixture-model supervised-machine-learning technique described in Ostrovski et al. (2017) applied to SDSS *u*, *g*, and *i*, and *Wide-field Infrared Survey Explorer* (*WISE*) *W*1 and *W*2 catalogue level photometry (Ostrovski et al. in preparation). The lensing nature was confirmed via optical spectroscopy with the Echellette Spectrograph and Imager (ESI) on the Keck telescope in 2016 December prior to the *HST* observations presented here and will be described in Ostrovski et al. (in preparation). Delchambre et al. (2018) report the independent discovery of this spectroscopically confirmed lensed system as a lensed quasar candidate using *Gaia* observations. The lens system resides in a dense environment with several other galaxies within close proximity. Part of the lensed arc from the extended source is noticeable in the F160W band in IR.

2.2.3 ATLAS J0259–1635

This lens system was discovered in VLT Survey Telescope (VST)-ATLAS survey from candidates selected with quasar-like *WISE* colours (Schechter et al. 2018). The source for this system is at redshift $z_{\rm s} = 2.16$ (Schechter et al. 2018).

2.2.4 DES J0405–3308

The discovery of this system is reported by Anguita et al. (2018). A complete or partial Einstein ring is noticeable in all the *HST* bands. The source redshift is $z_{\rm s} = 1.713 \pm 0.001$ (Anguita et al. 2018).

Table 1. Observation information and references for the lens systems.

| System name	Observation date	Total exposure time (s)			Reference
		F160W	F814W	F475X	
PS J0147+4630	2017 Sept 13	2196.9	1348.0	1332.0	Berghea et al. (2017)
SDSS J0248+1913	2017 Sept 5	2196.9	1428.0	994.0	Ostrovski et al. (in preparation), Delchambre et al. (2018)
ATLAS J0259−1635	2017 Sept 7	2196.9	1428.0	994.0	Schechter et al. (2018)
DES J0405−3308	2017 Sept 6	2196.9	1428.0	1042.0	Anguita et al. (2018)
DES J0408−5354	2018 Jan 17	2196.9	1428.0	1348.0	Lin et al. (2017); Diehl et al. (2017); Agnello et al. (2017)
DES J0420−4037	2017 Nov 23	2196.9	1428.0	1158.0	Ostrovski et al. (in preparation)
PS J0630−1201	2017 Oct 5	2196.9	1428.0	980.0	Ostrovski et al. (2018); Lemon et al. (2018)
SDSS J1251+2935	2018 Apr 26	2196.9	1428.0	1010.0	Kayo et al. (2007)
SDSS J1330+1810	2018 Aug 15	2196.9	1428.0	994.0	Oguri et al. (2008)
SDSS J1433+6007	2018 May 4	2196.9	1428.0	1504.0	Agnello et al. (2018a)
PS J1606−2333	2017 Sept 1	2196.9	1428.0	994.0	Lemon et al. (2018)
DES J2038−4008	2017 Aug 29	2196.9	1428.0	1158.0	Agnello et al. (2018c)
WISE J2344−3056	2017 Sept 9	2196.9	1428.0	1042.0	Schechter et al. (2017)
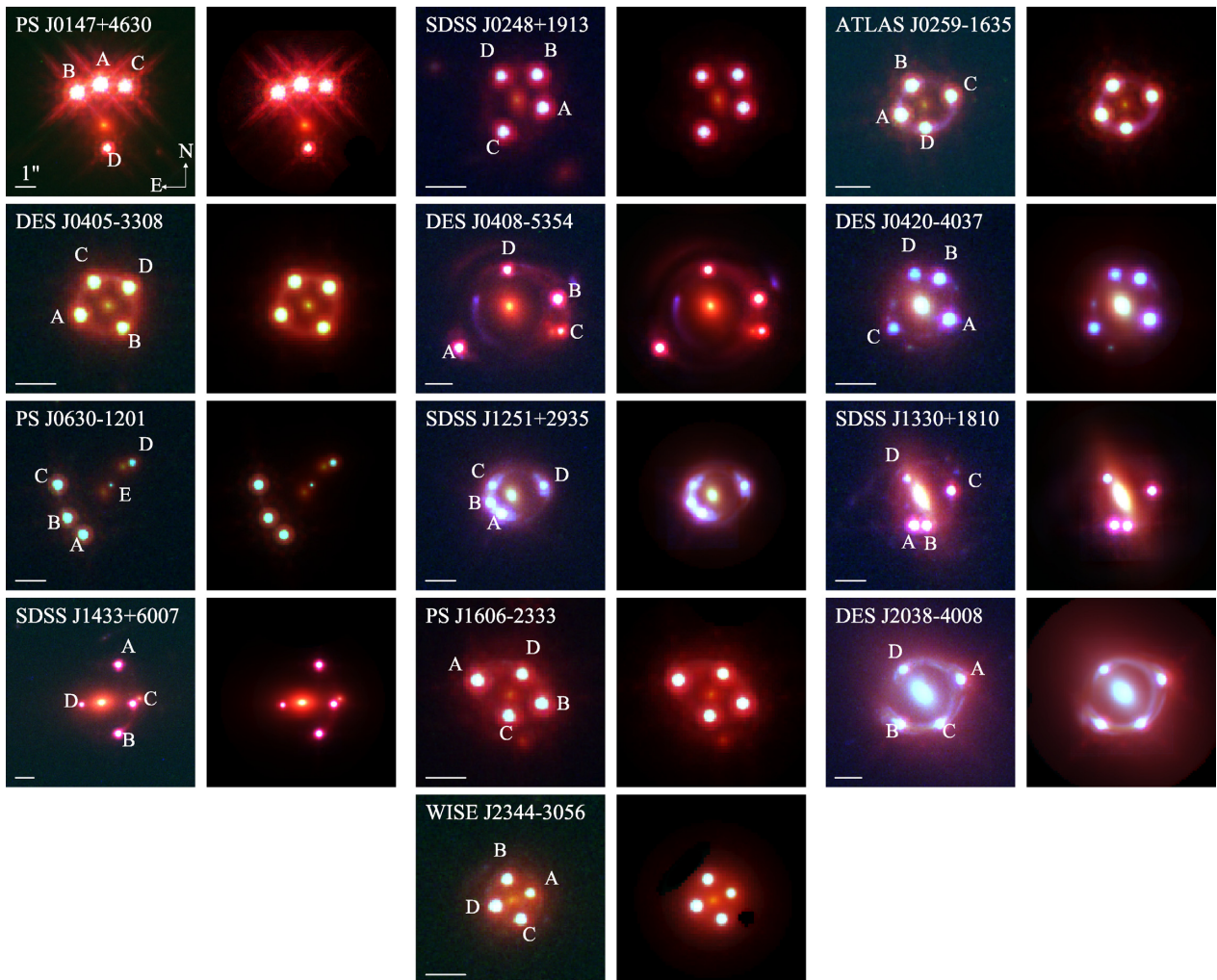
Figure 1. Comparison between the observed (first, third, and fifth columns) and reconstructed (second, fourth, and sixth columns) strong-lens systems. The three *HST* bands: F160W, F814W, and F475X are used in the red, green, and blue channels, respectively, to create the red-green-blue (RGB) images. Horizontal white lines for each system are rulers showing 1 arcsec. The relative intensities of the bands have been adjusted for each lens system for clear visualization of the features in the system.

2.2.5 DES J0408−5354

This system was discovered in the DES Year 1 data (Agnello et al. 2017; Diehl et al. 2017; Lin et al. 2017). The deflector redshift is $z_d = 0.597$ and the quasar redshift is $z_s = 2.375$ (Lin et al. 2017). This is a very complex lens system with multiple lensed arcs noticeable in addition to the quasar images. The sources of the lensed arcs can be components in the same source plane as the lensed quasar or they can be at different redshifts. This system has measured time-delays between the quasar images: $\Delta t_{AB} = -112 \pm 2.1$ d, $\Delta t_{AD} = -155.5 \pm 12.8$ d, and $\Delta t_{BD} = -42.4 \pm 17.6$ d (Courbin et al. 2018).

2.2.6 DES J0420−4037

This lens system was discovered in DES imaging data using the morphology-independent Gaussian-mixture-model supervised-machine-learning technique described in Ostrovski et al. (2017) applied to DES *g*, *r* and *i*, Visible and Infrared Survey Telescope for Astronomy (VISTA) *J* and *K*, and *WISE W*1 and *W*2 catalogue level photometry (Ostrovski et al. in preparation). Several small knots are noticeable near the quasar images that are possibly multiple images of extra components in the source plane.

2.2.7 PS J0630−1201

This system is a five-image lensed quasar system (Ostrovski et al. 2018). The discovery was the result of a lens search from *Gaia* data from a selection of lens candidates from Pan-STARRS and *WISE*. The source redshift is $z_s = 3.34$ (Ostrovski et al. 2018).

2.2.8 SDSS J1251+2935

This quad was discovered from the SDSS Quasar Lens Search (SQLS; Oguri et al. 2006; Inada et al. 2012) (Kayo et al. 2007). The source redshift is $z_s = 0.802$ and the deflector redshift is $z_d = 0.410$ measured from the SDSS spectra (Kayo et al. 2007).

2.2.9 SDSS J1330+1810

This lens system was also discovered from the SQLS (Oguri et al. 2008). The redshifts of the deflector and the source are $z_d = 0.373$ and $z_s = 1.393$, respectively (Oguri et al. 2008).

2.2.10 SDSS J1433+6007

This lens system was discovered in the SDSS data release 12 photometric catalogue (Agnello et al. 2018a). The redshifts of the source and deflector are $z_s = 2.737 \pm 0.003$ and $z_d = 0.407 \pm 0.002$, respectively (Agnello et al. 2018a).

2.2.11 PS J1606−2333

This quad was discovered from *Gaia* observations through a candidate search with quasar-like *WISE* colours over the Pan-STARRS footprint (Lemon et al. 2018). The main deflector has a noticeable companion near the southmost image.

2.2.12 DES J2038−4008

This lens system was discovered from a combined search in *WISE* and *Gaia* over the DES footprint (Agnello et al. 2018c). The deflector and the source redshifts are $z_d = 0.230 \pm 0.002$ and $z_s = 0.777 \pm 0.001$, respectively (Agnello et al. 2018c). This system has

an intricate Einstein ring with complex features from the extended quasar host galaxy.

2.2.13 WISE J2344−3056

This lens system was discovered in the VST-ATLAS survey (Schechter et al. 2017). This is a small-size quad with reported maximum image separation ∼1.1 arcsec. Several small and faint blobs are in close proximity, two of which are particularly noticeable near the north and east images.

3 LENS MODELLING

To devise a uniform approach that will suit a wide range of quads that vary in size, configuration, light profiles, etc., we need to choose from the most general models for the lens mass profile and the light distributions. It is often required to fine-tune the choice of models by adding complexities to the lens model in a case-by-case basis to suit the purpose of the specific science driver of an investigator. However, such detailed lens-modelling is outside of the scope of this paper. We only require our models to satisfactorily ($\chi^2_{red} \sim 1$) fit the data while being general enough to be applicable to a wide variety of lens systems.

We use the publicly available software package LENSTRONOMY[2] (Birrer & Amara 2018, based on Birrer et al. 2015) to model the quads in our sample. Prior to this work, LENSTRONOMY was used to measure the Hubble constant (Birrer, Amara & Refregier 2016) and to quantify lensing substructure (Birrer et al. 2017). We first adopt the simplest yet general set of profiles to model the deflector mass and light, and the source-light distributions (e.g. Sections 3.1 and 3.2). Then, we run a particle swarm optimization (PSO) routine through LENSTRONOMY to find the maximum of the likelihood function. After the PSO routine, we check for the goodness-of-fit of the best-fitting model. If the adopted profiles cannot produce an acceptable fit to the data, we gradually add more mass or light profiles to account for extra complexities in the lens system, e.g. presence of satellites, complex structure near the Einstein ring, or extra lensed source components. We run the PSO routine after each addition of complexity until a set of adopted mass and light profiles can produce an acceptable model. Next, we obtain the posterior probability distribution functions (PDFs) of the model parameters using a Markov chain Monte Carlo (MCMC) routine. The PSO and MCMC routines in LENSTRONOMY utilize the COSMOHAMMER package (Akeret et al. 2013). COSMOHAMMER itself embeds EMCEE (Foreman-Mackey et al. 2013), which is an affine-invariant ensemble sampler for MCMC (Goodman & Weare 2010) written in PYTHON.

In this section, we first describe the profiles used to parametrize the mass and light distributions. Then, we explain the decision tree of the modelling procedure.

3.1 Mass profile parametrization

We adopt a power-law elliptical mass distribution (PEMD) for the lens mass profile. This profile is parametrized as

$$\kappa = \frac{3-\gamma}{2}\left(\frac{\theta_E}{\sqrt{q\theta_1^2 + \theta_2^2/q}}\right)^{\gamma-1},\tag{1}$$

[2]https://github.com/sibirrer/lenstronomy

where γ is the power-law slope, θ_E is the Einstein radius, q is the axial ratio. The coordinates (θ_1, θ_2) depend on position angle ϕ through a rotational transformation of the on-sky coordinates that aligns the coordinate axes along the major and minor axes.

We also add an external shear profile parametrized by two parameters, γ_1 and γ_2. The external-shear magnitude γ_{ext} and angle ϕ_{ext} are related to these parameters by

$$\gamma_{ext} = \sqrt{\gamma_1^2 + \gamma_2^2}, \quad \tan 2\phi_{ext} = \frac{\gamma_2}{\gamma_1}. \qquad (2)$$

If there is a secondary deflector or a satellite of the main deflector, we choose an isothermal elliptical mass distribution (IEMD), which is a PEMD with the power-law slope γ fixed to 2.

3.2 Light profile parametrization

We choose the elliptical Sérsic function (Sérsic 1968) to model the deflector light profile. The Sérsic function is parametrized as

$$I(\theta_1, \theta_2) = I_e \exp\left[-k\left\{\left(\frac{\sqrt{\theta_1^2 + \theta_2^2/q_L^2}}{\theta_{eff}}\right)^{1/n_{Sersic}} - 1\right\}\right]. \qquad (3)$$

Here, I_e is the amplitude, k is a constant that normalizes θ_{eff} so that it is the half-light radius, q_L is the axial ratio, and n_{Sersic} is the Sérsic index. The coordinates (θ_1, θ_2) also depend on position angle ϕ_L that rotationally transforms the on-sky coordinates to align the coordinate axes with the major and minor axes. We add a 'uniform' light profile parametrized by only one parameter, the amplitude, that can capture unaccounted flux from the lens by a single Sérsic profile.

The circular Sérsic function (with $q_L = 1$, $\phi_L = 0$) is adopted to model the host-galaxy-light distribution. We limit $\theta_{eff} > 0\overset{''}{.}04$ (which is the pixel size in the UVIS bands) on the source plane to prevent the Sérsic profile to be too pointy effectively mimicking a point source. For a typical source redshift $z_s = 2$, 0.04 arcsec corresponds to ~0.33 kpc. This is a reasonable lower limit for the size of a lensed source hosting a supermassive black hole. If there are complex structures in the lensed arcs that cannot be fully captured by a simple Sérsic profile, we add a basis set of shapelets (Refregier 2003; Birrer et al. 2015) on top of the Sérsic profile to reconstruct the source-light distribution. The basis set is parametrized by maximum order n_{max}, and a characteristic scale β. The number of shapelets is given by $(n_{max} + 1)(n_{max} + 2)/2$.

The quasar images are modelled with point sources with a point spread function (PSF) on the image plane.

3.3 Modelling procedure

We model the quads in a general framework to simultaneously fit the data from all three *HST* bands. Fig. 2 illustrates the flow of the modelling procedure. We describe the nodes of this flow chart below. Each node is marked with a lowercase letter. Some of the decision nodes in Fig. 2 are self-explanatory and need no further elaboration.

a. Initial set-up: We first pre-process the data in each band. A cut-out with an appropriate field-of-view covering the lens and nearby environment from the whole image is chosen. The background flux estimated by SEXTRACTOR (Bertin & Arnouts 1996) from the whole image is subtracted from the cutout. We also select four or more stars from the *HST* images to estimate the initial PSF in each band. A circular mask with a suitable radius is chosen to only include the deflector-light distribution, and the lensed quasar-images and

arcs. If there is a nearby galaxy or a star, we mask it out unless we specifically choose to model the light profile of a satellite or companion galaxy, e.g. for DES J0408−5354, PS J0630−1201, SDSS J1433+6007, and PS J1606−2333. As PS J0630−1201 is a five-image lens, we allow the model the flexibility to produce more than four images.

b. Fit the 'most informative' band: It is important to judiciously initiate any optimization routine, such as the PSO, to efficiently find the global extremum. Finding the global maximum of the joint likelihood from all the bands together from a random initial point is often very expensive in terms of time and computational resource. Therefore, we first only fit the 'most informative' band to iteratively select the light and mass profiles necessary to account for the lens complexity. In this study, we choose F814W as the 'most informative' band. It is easier to decompose the deflector and the source-light distributions in the F814W band than in the F160W band as the deflector does not have a large flux near or beyond the Einstein ring. The resolution in the F814W band is also twice as high as in the F160W band. Furthermore, the deflector flux in the F475X band is often too small to reliably model the deflector-light distribution without a good prior. At first, we fix the power-law slope for the lens mass model at $\gamma = 2$ (i.e. the isothermal case). With each consecutive PSO routine, we narrow down the search region in the parameter space around the maximum of the likelihood. After each PSO routine, we iteratively reconstruct the PSF with the modelled-extended-light subtracted quasar images themselves. This is performed iteratively such that the extended light model updates its model with the new PSF to avoid biases and overconstraints on the PSF model. Similar procedures have been used in Chen et al. (2016), Birrer et al. (2017), and Wong et al. (2017). The details are described in Birrer et al. (2019) and the reconstruction routines are part of LENSTRONOMY.

c. Good fit? We check for the goodness of fit by calculating the p-value for the total χ^2 and degrees of freedom. We set p-value $\gtrsim 10^{-8}$ as a criterion to accept a model. This low p-value is enough to point out substantial inadequacies in the model while applicable to the wide variety of the lens systems in our sample. Implementing a higher p-value would require noise-level modelling that is hard to achieve in a uniform framework. The total χ^2 in this node is computed from the residuals in the F814W band only.

e. Add satellite mass profile: We add an IEMD for the satellite or companion mass profile. The light distribution of the satellite is modelled with an elliptical Sérsic profile. The initial centroid of the satellite is chosen approximately at the centre of the brightest pixel in the satellite.

g. Add extra source component: If there are extra lensed source components, e.g. blobs or arcs, that are not part of the primary source structure near the Einstein ring, we add extra light profiles in the same source plane of the lensed quasar. We only add one light profile for each set of conjugate components. It is easier to identify and constrain the positions of additional source components on the image plane. Among the identifiable conjugate components from visual inspection, if one component is a smaller blob, and the others form arcs, we choose the blob's position in the image plane as the initial guess. First, we only add one circular Sérsic profile for each additional source component. For the second visit to this node, i.e. there is unaccounted structure or extra light near the additional lensed source components, we add shapelets with $n_{max} = 3$ on top of the Sérsic profile. For each subsequent visit, we increase n_{max} by 2.

h. Add shapelets to source-light profile: If there are structures near the Einstein ring, we add a basis set of shapelets on top of
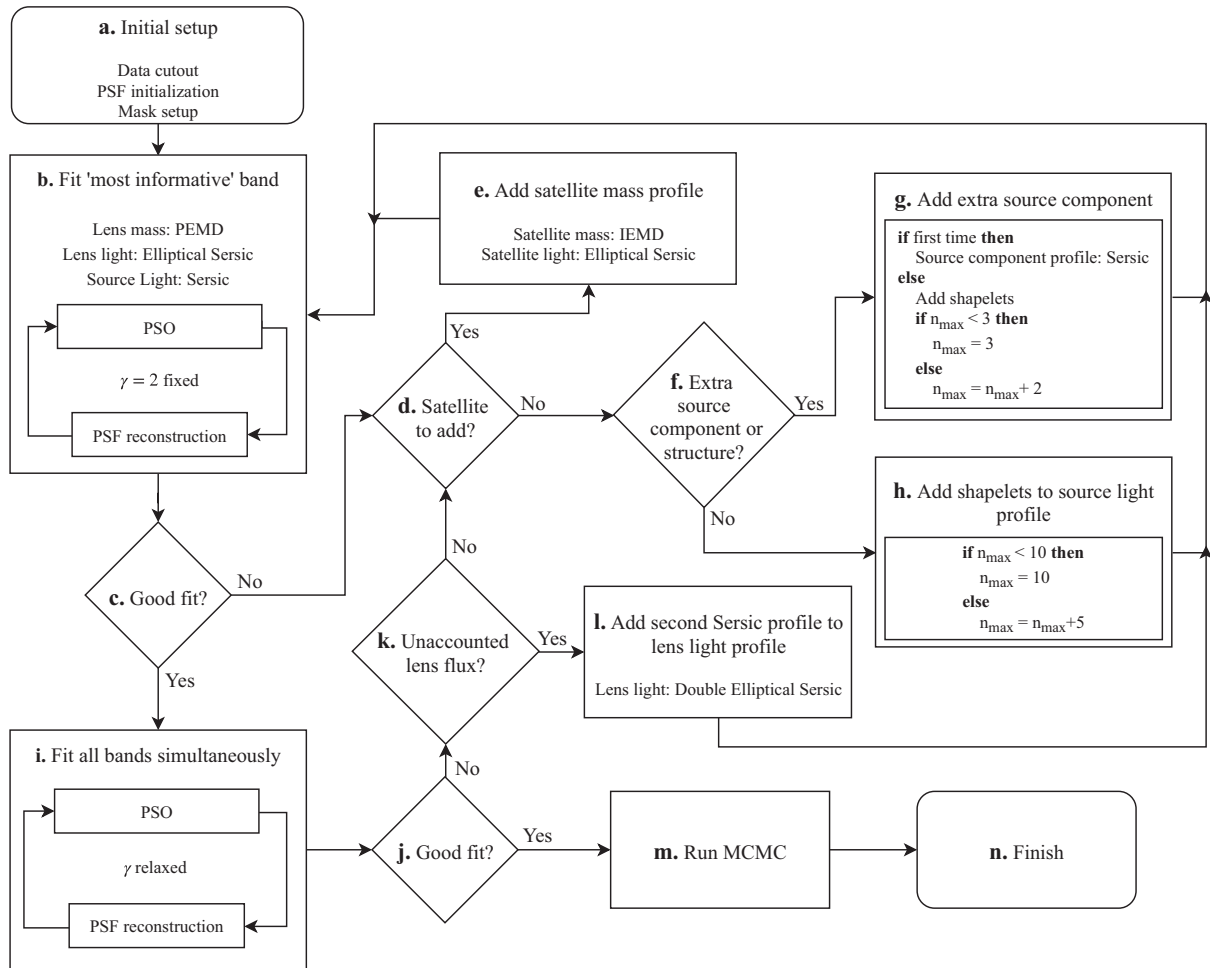
a. Initial setup

Data cutout
PSF initialization
Mask setup

b. Fit 'most informative' band

Lens mass: PEMD
Lens light: Elliptical Sersic
Source Light: Sersic

PSO
$\gamma = 2$ fixed
PSF reconstruction

c. Good fit? — No / Yes

e. Add satellite mass profile

Satellite mass: IEMD
Satellite light: Elliptical Sersic

d. Satellite to add? — Yes / No

f. Extra source component or structure? — Yes / No

g. Add extra source component

if first time **then**
    Source component profile: Sersic
else
    Add shapelets
    if $n_{\max} < 3$ **then**
        $n_{\max} = 3$
    else
        $n_{\max} = n_{\max} + 2$

h. Add shapelets to source light profile

if $n_{\max} < 10$ **then**
    $n_{\max} = 10$
else
    $n_{\max} = n_{\max}+5$

k. Unaccounted lens flux? — Yes / No

l. Add second Sersic profile to lens light profile

Lens light: Double Elliptical Sersic

i. Fit all bands simultaneously

PSO
γ relaxed
PSF reconstruction

j. Good fit? — Yes

m. Run MCMC

n. Finish

Figure 2. Flowchart showing the decision tree for uniform modelling of quads to simultaneously fit multiband data. After the initial set-up (node a), the fitting is first done only with one band (node b) to iteratively choose the necessary level of complexity in the mass and light profiles (nodes d, e, f, g, h, k, l). A proposed model is accepted, if the power-law slope γ does not diverge to a bound of the allowed range (nodes j) and the p-value $\gtrsim 10^{-8}$ for the fit (nodes c, j). After deciding upon a set of profiles to simultaneously model the multiband data (node i), the uncertainties on the model parameters are obtained by running a MCMC routine (node m).

the Sérsic function to the primary source-light profile. We first add shapelets with $n_{\max} = 10$ and increase $n_{\max}$ by 5 for each future visit to this node. The characteristic scale β of the shapelets is initiated with the best fit θ_{eff} of the Sérsic profile for the source.

i. Fit all bands simultaneously: Before fitting all the bands simultaneously it is important to check astrometric alignment between the bands and correct accordingly if there is a misalignment. We align the data from the IR channel (F160W) with those from the UVIS band (F814W and F475X) by matching the positions of the four lensed quasar images. After that, we run PSO routines to fit all the bands simultaneously. Each PSO routine is followed by one iterative PSF reconstruction routine. During simultaneous fitting, only the intensities of the light profiles and shapelets are varied independently for different bands. All the other parameters, such as scalelength, ellipticity, position angle and Sérsic index, are set to be common across wavelengths, which is a common practice for simultaneous fitting of multiband data (e.g. Stoughton et al. 2002; Lackner & Gunn 2012). As a result, for the case of a single Sérsic profile the best-fitting parameters are effectively an average over the wavelengths. However, we find the resultant best-fitting parameters

from the simultaneous fitting to be within 1σ systematic+statistical uncertainty of the ones from the individual fits of different bands for one representative system (DES J0405$-$3308) from our sample. Therefore, we assume that setting these parameters to be common across wavelengths is sufficient for the purpose of this study. For the case of shapelets or double Sérsic profile, the relative intensities of the shapelets or Sérsic components can freely vary across bands. This allows for more complex morphological variation across wavelengths and makes our assumption even more reasonable.

j. Good fit? We check for the goodness of fit with the same criteria described in node c. In this node, the total χ^2 is computed from the residuals in all the three bands. Moreover, we check that the power-law slope γ has not diverged to the bound of the allowed values when γ is relaxed in node i. This might happen if there is not enough complexity in the adopted model to reconstruct the observed fluxes. We also check if there is lens flux unaccounted by the single Sérsic profile. If the total flux in the 'uniform' light profile within the effective radius is more than one per cent of that for the elliptical Sérsic profile, we decide that there is unaccounted

lens flux. This can particularly happen in the F160W band as the lens light is more extended in the IR than in the UVIS channels and two concentric Sérsic functions provide a better fit to the lens light (Claeskens et al. 2006; Suyu et al. 2013). If there is no unaccounted lens light, we discard the 'uniform' profile from the set of lens-light profiles before moving to node m.

l. Add second Sérsic function to lens-light profile: If there is unaccounted lens flux, we discard the 'uniform' light profile and add a second Sérsic function on top of the first one with the same centroid. We fix the Sérsic indices for the two Sérsic profiles to $n_{\text{Sérsic}} = 4$ (de Vaucouleurs profile) and $n_{\text{Sérsic}} = 1$ (exponential). We fix these Sérsic indices for numerical stability. These profile fits should not be interpreted as bulge–disc decompositions. For a proper bulge–disc decomposition, more robust methods should be adopted to detect the presence of multiple components, e.g. Bayesian model comparison (D'Souza et al. 2014) and axis-ratio variation technique (Oh, Greene & Lackner 2017).

m. Run MCMC: If the PSO fitting sequence finds an acceptable model for the quad, we run an MCMC routine. The initial positions of the walkers are centred around the best fit found by the PSO fitting sequence.

n. Finish: After the MCMC routine, we check for the convergence of the chain. We accept the chain as converged, if the total number of steps is $\sim$10 times the autocorrelation length, and the median and variance of the walker positions at each step are stable for 1 autocorrelation length at the end of the chain. We then calculate the best-fitting value for each model parameter from the median of the walker positions at the last step. Similarly, 1σ confidence levels are computed from the 16th and 84th percentiles in the last step.

3.4 Systematics

We estimate the systematic uncertainties of the lens model parameters by marginalizing over several numerical settings. We performed the modelling technique described in Section 3.3 with 11 different numerical settings: varying the lens-mask size, varying the mask size for extra quasar-images for PSF reconstruction, varying the sampling resolution of the reconstructed *HST* image, without PSF reconstruction, and with different realisations of the reconstructed PSF. We checked for systematics for the lens system SDSS J0248+1913. This system was chosen for two reasons: (i) this system has relatively fainter arc compared to the point source and deflector brightness, thus providing a conservative estimate of the systematics, and (ii) the modelling procedure is one of the simplest ones that enables running the modelling procedure numerous times with different settings in relatively less time. We assume the systematics are the same order of magnitude for the other lens systems in the sample.

4 RESULTS

In this section, we first describe the lens models and report the model parameters along with some derived parameters for all the quads. Then, we investigate the alignment between the mass and light profiles and report our findings. In Appendices A–C, we report additional inferred lens model parameters that are not directly relevant for the scientific investigation carried out here but may be of interest to some readers, especially in planning future follow-up and observations.

4.1 Efficiency of the uniform framework

All the 13 quads are reliably (p-value $\sim$ 1; Table 2) modelled following the uniform approach described in Section 3.3. The framework was designed and tuned from the experience gained from uniformly modelling the first ten observed quads in the sample. The three quads, SDSS J1251+2935, SDSS J1330+1810 and SDSS J1433+6007, were observed after the design phase. We effectively modelled these three lenses implementing the general framework, which validates its effectiveness. The total investigator time spent for these two lenses is $\sim$3 h per lens including data reduction, initial set-up and quality control of the model outputs. The number of CPU hours (on state-of-the-art machines[3]) per system ranges between 50 and 500 depending on the complexity of the model.

4.2 Lens models

The set of profiles chosen through the decision tree for modelling the quads along with the corresponding p-values are listed in Table 2. We show a breakdown of the best-fitting models in each band for the quads, SDSS J0248+1913, DES J0408-5354, SDSS J1251+2935, SDSS J1433+6007, as examples, in Fig. 3. Model breakdowns for the rest of lenses are provided in Appendix D. We show the red-green-blue (RGB) images produced from the *HST* data alongside the reconstructed RGB images for all the quads in Fig. 1.

We checked the robustness of the estimated lens model parameters with and without PSF reconstructions. We find the Einstein radius θ_{E}, axial ratio q, mass position angle ϕ, external shear γ_{ext}, and shear angle ϕ_{ext} to be robustly (within 1σ systematic+statistical uncertainty) estimated. However, the power-law slope γ is affected by $\geq 1\sigma$ systematic+statistical uncertainty due to deviations of the reconstructed PSF. This is expected as γ depends on the thickness of the Einstein ring and this thickness in the reconstructed model in turn depends on the PSF.

We investigated if setting the Sérsic radius and index of the source light profile common across wavelength bands biases the measurement of the power-law slope. For one representative system (DES J0405+3308) from our sample, we find the power-law slope from the individual fits of different bands to agree within 1σ systematic+statistical uncertainty of the one from the simultaneous fit. Therefore, we conclude that setting the scaling parameters of the source light profile except the intensity to be common across wavelengths does not significantly ($>1\sigma$) bias the power-law slope.

We checked if the lens model parameters are stable with increasing complexity in the model (Fig. 4). The stability of the Einstein radius θ_{E} and the external shear γ_{ext} improves if the mass profile of a satellite is explicitly modelled. For increasing complexity in modelling the source-light distribution, the power-law slope γ, the Einstein radius θ_{E}, and the external convergence γ_{ext} are stable.

We report the lens model parameters: Einstein radius θ_{E}, power-law slope γ, axial ratio q, position angle ϕ, external shear γ_{ext}, and shear angle ϕ_{ext} and deflector light parameters: effective radius θ_{eff}, axial ratio q_{L}, and position angle ϕ_{L} in Table 3. For the deflectors fitted with double Sérsic profiles, the ellipticity and position angles are computed by fitting isophotes to the double Sérsic light distri-

---

[3]We utilized the Hoffman2 Shared Cluster provided by UCLA Institute for Digital Research and Education's Research Technology Group. https://idre.ucla.edu/hoffman2.

Table 2. Lens model profiles.

System name	Mass profiles	Lens-light profiles	Source-light profiles	p-value[a]	Decision flow[b]
PS J0147+4630	PEMD	Double elliptical Sérsic	Sérsic	1.0	abcijklbcijmn
			Point source (image plane)		
SDSS J0248+1913	PEMD	Elliptical Sérsic	Sérsic	1.0	abcijmn
			Point source (image plane)		
ATLAS J0259−1635	PEMD	Elliptical Sérsic	Sérsic	1.0	abcdfhbcijmn
			Shapelets ($n_{max} = 10$)		
			Point source (image plane)		
DES J0405−3308	PEMD	Elliptical Sérsic	Sérsic	1.0	abcijmn
			Point source (image plane)		
DES J0408−5354	PEMD	Elliptical Sérsic	Sérsic	1.0	abcdebcdfgbcdfgbcijkdf
	IEMD[c]	Elliptical Sérsic[c]	Shapelets ($n_{max} = 10$)		gbcijkdfhbcijmn
			Sérsic[c]		
			Shapelets[c] ($n_{max} = 3$)		
			Sérsic[c]		
			Point source (image plane)		
DES J0420−4037	PEMD	Elliptical Sérsic	Sérsic	1.0	abcijkdfgbcijmn
			Sérsic[c]		
			Sérsic[c]		
			Point source (image plane)		
PS J0630−1201	PEMD	Elliptical Sérsic	Sérsic	1.0	abcdebcijmn
	IEMD[c]	Elliptical Sérsic[c]	Point source (image plane)		
SDSS J1251+2935	PEMD	Double elliptical Sérsic	Sérsic	1.0	abcijklbcijkdfhbcijmn
			Shapelets ($n_{max} = 10$)		
			Point source (image plane)		
SDSS J1330+1810	PEMD	Double elliptical Sérsic	Sérsic	0.005	abcijklbcijkdfhbcijmn
			Shapelets ($n_{max} = 10$)		
			Point source (image plane)		
SDSS J1433+6007	PEMD	Double elliptical Sérsic	Sérsic	1.0	abcdebcijklbcijmn
	IEMD[c]	Elliptical Sérsic[c]	Point source (image plane)		
PS J1606−2333	PEMD	Double elliptical Sérsic	Sérsic	1.0	abcdebcdfhbcijklbcijmn
	IEMD[c]	Elliptical Sérsic[c]	Shapelets ($n_{max} = 10$)		
			Point source (image plane)		
DES J2038−4008	PEMD	Double elliptical Sérsic	Sérsic	1.0	abcdfhbcijklbcijmn
			Shapelets ($n_{max} = 10$)		
			Point source (image plane)		
WISE J2344−3056	PEMD	Double elliptical Sérsic	Sérsic	1.0	abcijklbcijmn
			Point source (image plane)		

Notes. [a]The p-value is for the combined χ^2 from all three bands.
[b]Labels of nodes visited during the modelling procedure in the flow chart shown in Fig. 2.
[c]Satellite or extra source component separate from the central source.

bution. We use the PHOTUTILS[4] package in PYTHON for measuring the isophotes that implements an iterative method described by Jedrzejewski (1987). We tabulate the astrometric positions of the deflector galaxy and the quasar images in Table 4. The apparent magnitudes of the deflector galaxy and the quasar images in each of the three *HST* bands are given in Table 5.

4.3 Alignment between mass and light distributions

In this subsection, we report our results on the alignment between the mass and light distributions in our sample of quads (Fig. 5).

4.3.1 Centroid

The centres of the mass and light distributions match very well for most of the quads with a root-mean-square (rms) of 0.04 excluding

[4]http://photutils.readthedocs.io

three outliers (Fig. 5a). The three outliers are PS J0147+4630, DES J0408-5354, and PS J0630−1201. In PS J0630−1201, there are two deflectors with comparable mass creating a total of five images. If the two deflectors are embedded in the same dark matter halo, the centre of the luminous part of the deflector can have an offset from the centre of the halo mass. The other two outliers also have nearby companions possibly biasing the centroid estimation.

4.3.2 Ellipticity

We find a weak correlation between the ellipticity parameters of the mass and light distribution for the whole sample (Fig. 5b). We calculate the Pearson correlation coefficient between the axis ratios q and q_L of the mass and light distributions, respectively, in the following way. We sample 1000 points from a two-dimensional Gaussian distribution that is centred on the axial ratio pair (q, q_L) for each quad. We take the standard deviation for this Gaussian distribution along each axis equal to the 1σ systematic+statistical uncertainty. We take the covariance between the sampled points
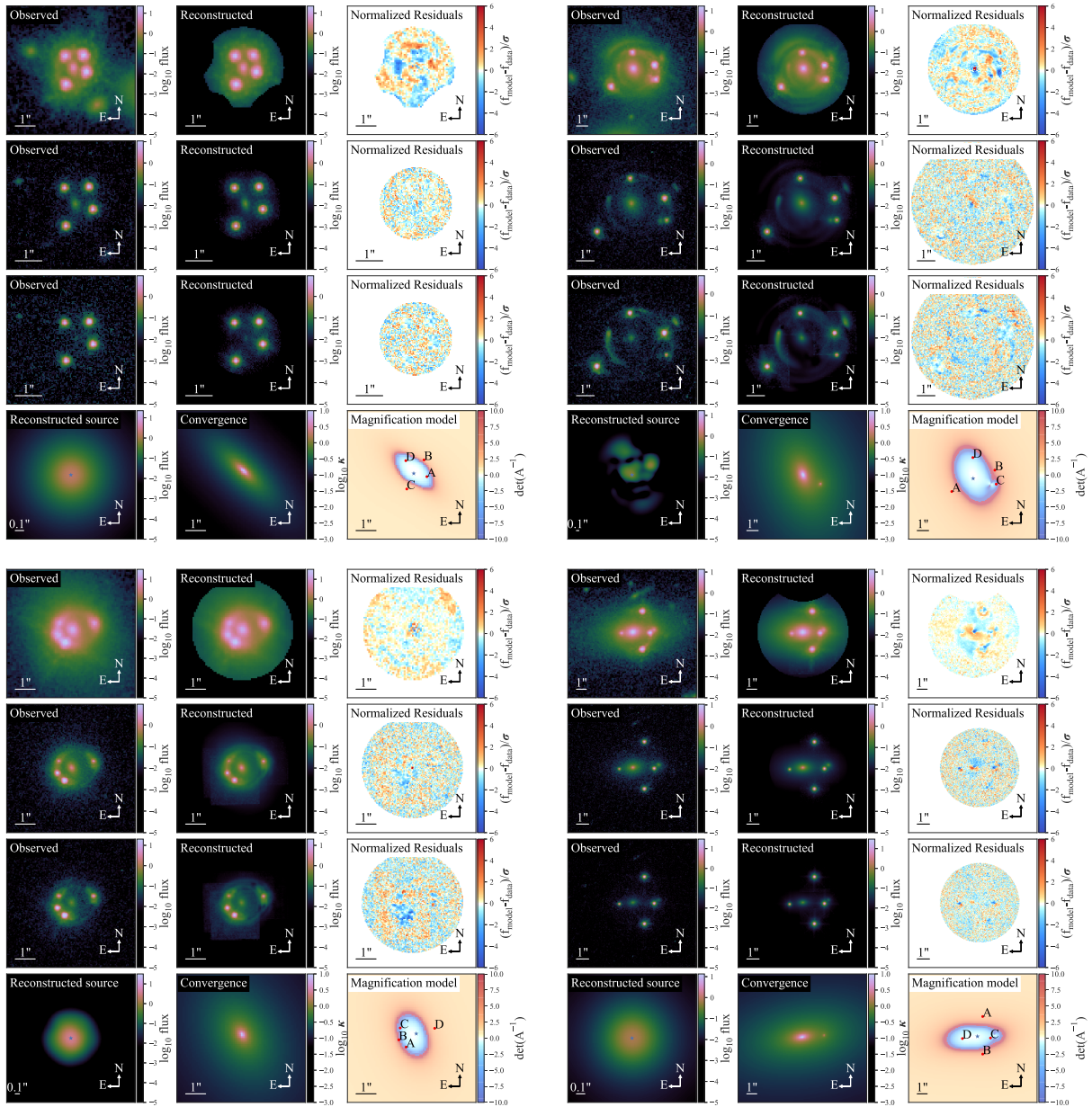
Figure 3. Best-fitting models for SDSS J0248+1913 (top left), DES J0408-5354 (top right), SDSS J1251+2935 (bottom left), and SDSS J1433+6007 (bottom right). The first three rows for each lens system show the observed image, reconstructed lens image, and the normalized residuals in three *HST* bands: F160W, F814W, and F475X, respectively. The fourth row shows the reconstructed source in the F160W band, the convergence, and the magnification model. The models for the rest of the sample are shown in Appendix D (Figs D1 and D2).

for each lens as zero as we observe no degeneracy in the posterior PDF of the axis ratios for individual lenses. The Pearson correlation coefficient for the distribution of the sampled points from all the quads is $r = 0.2$ (weak correlation).

4.3.3 Position angle

The position angles of the elliptical mass and light distributions are well aligned for 9 out of 13 quads. The standard deviation of the misalignment in position angles for these eight lenses is $11°$ (Fig. 5c). The systems with large misalignment also have large external shear. We find a strong correlation between the misalignment angle and the external shear magnitude ($r = 0.74$,

Fig. 5d). We find weak correlation between the misalignment angle and the mass axial ratio q ($r = 0.21$, Fig. 5e).

4.4 Deviation of flux ratios from macro-model

Stars or dark subhaloes in the deflector can produce additional magnification or de-magnification of the quasar images through microlensing and millilensing, respectively (for detailed description, see Schneider, Kochanek & Wambsganss 2006). In that case, the flux ratios of the quasar images will be different than those predicted by the smooth macro-model. Deviation of the flux ratios can also be produced by baryonic structures (Gilman et al. 2017) or discs (Hsueh et al. 2016, 2017), quasar variability with a time delay,
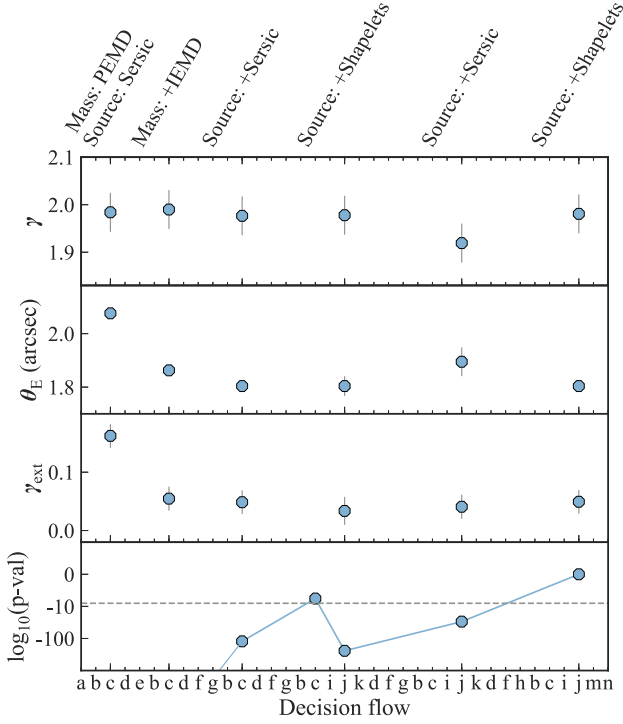
Figure 4. Stability of lens model parameters with increasing model complexity. The four panels show the power-law slope γ, Einstein radius θ_E, external shear γ_{ext}, and logarithm of p-value of the reduced-χ^2 of the model fit, top to bottom, along the decision-flow for the quad DES J0408−5354. The bottom-horizontal axis denotes the node identifiers along the decision flow as in Fig. 2. Short descriptions for added profiles at corresponding points along the decision flow are shown along the top-horizontal axis. Solid-grey lines attached to the blue circles show 1σ systematic+statistical uncertainty. The dashed-grey line at the bottom panel marks the threshold p-value $= 10^{-8}$ for accepting a model. The p-value decreases after crossing the threshold the first time due to addition of the other two bands for simultaneous fitting, which requires more complexity in the model.

and dust extinction (Yonehara, Hirashita & Richter 2008; Anguita et al. 2008). We quantify this deviation of the flux ratios in the

quasar images as a χ^2-value by

$$\chi_f^2 = \sum_{\substack{I,J \in \{A,\ B,\ C,\ D\}}}^{I \neq J} \frac{\left(f_{IJ,\ observed} - f_{IJ,\ model}\right)^2}{\sigma_{f_{IJ}}^2}, \qquad (4)$$

where $f_{IJ} = F_I/F_J$ is the flux ratio between the images I and J. We assume 20 per cent flux error giving $\sigma_{f_{IJ}} = 0.28 f_{IJ}$. We set this error level considering the typical order of magnitude for intrinsic variability of quasars (e.g. Bonvin et al. 2017; Courbin et al. 2018). Although, many of the quads in our sample have short predicted time-delays (Table C1), where intrinsic variability is not a major source of deviation in flux-ratios, we take 20 per cent as a conservative error estimate for these lenses.

If the flux ratios are consistent with the macro-model, χ_f^2 is expected to follow the $\chi^2(3)$ distribution, i.e. $\chi_f^2 \sim \chi^2(3)$, as only three out of the six flux ratios are independent producing three degrees of freedom. However, the χ_f^2-distribution is shifted toward a higher value than $\chi^2(3)$ (Fig. 6). The mean of the combined distribution of $\log_{10} \chi_f^2$ from all the three *HST* bands is 2.04. A Kolmogorov–Smirnov test of whether the observed χ_f^2-distribution matches with the $\chi^2(3)$-distribution yields a p-value of ~ 0. The shift is higher in shorter wavelengths. The mean of the $\log_{10} \chi_f^2$'s in the F160W, F814W, and F475X bands are 1.85, 2.09, and 2.17, respectively. This is expected, as the quasar size is smaller in shorter wavelengths making it more affected by microlensing, and as shorter wavelengths are also more affected by dust extinction.

5 SUMMARY AND DISCUSSION

We presented a general framework to uniformly model large samples of quads while attempting to minimize investigator time. We apply this framework to model a sample of 13 quads and simultaneously fit imaging data from three *HST* WFC3 bands. All the quads are satisfactorily (p-value $\gtrsim 10^{-8}$) modelled in our uniform framework. We choose the p-value threshold to be suitably low to be applicable to our quad sample with large morphological variation while being able to point out deficiencies in the modelling choice of profiles along the decision tree. In the end, most of the lens systems in our sample are modelled with p-value ~ 1 (Table 2). Thus, we showed that a large variety of quads can be modelled with a basic set of mass and light profiles under our framework, i.e. all the quads in our sample are 'happy' (or, at least 'content').

Table 3. Lens model parameters. The reported uncertainties are systematic and statistical uncertainties added in quadrature.

System name	θ_E (arcsec)	γ	q	ϕ (E of N) (deg)	γ_{ext}	ϕ_{ext} (E of N) (deg)	$\theta_{eff}{}^a$ (arcsec)	$q_L{}^a$	ϕ_L (E of N)^a (deg)
PS J0147+4630	1.90 ± 0.01	2.00 ± 0.05	0.81 ± 0.04	-55 ± 6	0.16 ± 0.02	-72 ± 3	3.45 ± 0.10	0.93 ± 0.06	49 ± 16
SDSS J0248+1913	0.804 ± 0.004	2.19 ± 0.04	0.40 ± 0.06	46 ± 6	0.09 ± 0.02	6 ± 3	0.16 ± 0.03	0.40 ± 0.02	13 ± 1
ATLAS J0259−1635	0.75 ± 0.01	2.01 ± 0.04	0.66 ± 0.04	18 ± 6	0.00 ± 0.02	-30 ± 3	1.00 ± 0.09	0.38 ± 0.04	20 ± 4
DES J0405−3308	0.70 ± 0.01	1.99 ± 0.04	0.95 ± 0.05	41 ± 12	0.01 ± 0.02	-79 ± 5	0.44 ± 0.09	0.55 ± 0.05	37 ± 4
DES J0408−5354	1.80 ± 0.01	1.98 ± 0.04	0.62 ± 0.04	18 ± 6	0.05 ± 0.02	-15 ± 3	2.15 ± 0.09	0.82 ± 0.04	28 ± 4
DES J0420−4037	0.83 ± 0.01	1.97 ± 0.04	0.87 ± 0.04	24 ± 6	0.03 ± 0.02	-20 ± 4	0.44 ± 0.09	0.61 ± 0.04	27 ± 4
PS J0630−1201	1.02 ± 0.01	2.00 ± 0.04	0.53 ± 0.04	-27 ± 6	0.14 ± 0.02	-2 ± 3	1.64 ± 0.09	0.79 ± 0.04	12 ± 4
SDSS J1251+2935	0.84 ± 0.01	1.97 ± 0.04	0.71 ± 0.04	28 ± 6	0.07 ± 0.02	-88 ± 3	1.02 ± 0.09	0.67 ± 0.04	23 ± 4
SDSS J1330+1810	0.954 ± 0.005	2.00 ± 0.04	0.59 ± 0.06	24 ± 6	0.07 ± 0.02	8 ± 3	0.40 ± 0.03	0.28 ± 0.02	24 ± 1
SDSS J1433+6007	1.71 ± 0.01	1.96 ± 0.04	0.51 ± 0.04	-81 ± 6	0.09 ± 0.02	-30 ± 3	1.10 ± 0.09	0.56 ± 0.04	-88 ± 4
PS J1606−2333	0.63 ± 0.01	1.97 ± 0.04	0.88 ± 0.05	41 ± 10	0.16 ± 0.02	53 ± 3	1.36 ± 0.09	0.60 ± 0.07	-24 ± 5
DES J2038−4008	1.38 ± 0.01	2.35 ± 0.04	0.61 ± 0.04	38 ± 6	0.09 ± 0.02	-58 ± 3	2.85 ± 0.09	0.67 ± 0.04	38 ± 4
WISE J2344−3056	0.52 ± 0.01	1.95 ± 0.05	0.51 ± 0.06	-70 ± 6	0.06 ± 0.02	-68 ± 8	2.61 ± 0.19	0.76 ± 0.03	-69 ± 4

Note. ^{a}Calculated from the F160W band for the lenses with double Sérsic fit for the lens light.

Table 4. Astrometric positions of the deflector and quasar images. The reported uncertainties are on relative astrometry and they are systematic and statistical uncertainties added in quadrature.

System name	Deflector		Image A		Image B		Image C		Image D	
	α (deg)	δ (deg)	$\Delta\alpha$ (arcsec)	$\Delta\delta$ (arcsec)	$\Delta\alpha$ (arcsec)	$\Delta\delta$ (arcsec)	$\Delta\alpha$ (arcsec)	$\Delta\delta$ (arcsec)	$\Delta\alpha$ (arcsec)	$\Delta\delta$ (arcsec)
PS J0147+4630	26.792331	46.511559	-0.0046 ± 0.0002	2.0649 ± 0.0001	1.1671 ± 0.0002	1.6555 ± 0.0002	-1.2439 ± 0.0002	1.9716 ± 0.0002	-0.3462 ± 0.0005	-1.1560 ± 0.0003
SDSS J0248+1913	42.203099	19.225246	-0.787 ± 0.001	-0.175 ± 0.001	-0.645 ± 0.001	0.658 ± 0.001	0.211 ± 0.001	-0.791 ± 0.001	0.261 ± 0.001	0.620 ± 0.001
ATLAS J0259−1635	44.928561	−16.595376	0.602 ± 0.003	-0.216 ± 0.001	0.275 ± 0.001	0.658 ± 0.001	-0.883 ± 0.001	0.340 ± 0.001	-0.124 ± 0.001	-0.614 ± 0.001
DES J0405−3308	61.498964	−33.147417	0.536 ± 0.001	-0.155 ± 0.001	-0.533 ± 0.001	-0.478 ± 0.001	0.186 ± 0.002	0.686 ± 0.002	-0.684 ± 0.001	0.538 ± 0.004
DES J0408−5354	62.090451	−53.899816	1.981 ± 0.002	-1.495 ± 0.001	-1.775 ± 0.001	0.369 ± 0.001	-1.895 ± 0.002	-0.854 ± 0.002	0.141 ± 0.001	1.466 ± 0.002
DES J0420−4037	65.194858	−40.624081	-0.698 ± 0.001	-0.231 ± 0.001	-0.457 ± 0.001	0.802 ± 0.001	0.711 ± 0.001	-0.448 ± 0.001	0.172 ± 0.002	0.908 ± 0.002
PS J0630−1201[a]	97.537601	−12.022037	0.613 ± 0.001	-1.349 ± 0.001	1.131 ± 0.001	-0.783 ± 0.001	1.470 ± 0.001	0.337 ± 0.001	-1.050 ± 0.001	1.082 ± 0.001
SDSS J1251+2935	192.781427	29.594652	0.3370 ± 0.0005	-0.6245 ± 0.0005	0.698 ± 0.001	-0.265 ± 0.001	0.628 ± 0.001	0.327 ± 0.001	-1.089 ± 0.001	0.310 ± 0.002
SDSS J1330+1810	202.577755	18.175788	0.247 ± 0.001	-1.025 ± 0.001	-0.179 ± 0.001	-1.049 ± 0.001	-1.013 ± 0.001	0.133 ± 0.001	0.4938 ± 0.0004	0.550 ± 0.002
SDSS J1433+6007	218.345420	60.120777	-0.960 ± 0.002	2.070 ± 0.002	-0.962 ± 0.003	-1.679 ± 0.003	-1.740 ± 0.002	-0.072 ± 0.002	1.056 ± 0.003	-0.127 ± 0.003
PS J1606−2333	241.500982	−23.556114	0.856 ± 0.001	0.298 ± 0.001	-0.769 ± 0.001	-0.298 ± 0.001	0.064 ± 0.001	-0.616 ± 0.001	-0.272 ± 0.001	0.449 ± 0.001
DES J2038−4008	309.511379	−40.137024	-1.529 ± 0.001	0.495 ± 0.001	0.7867 ± 0.0005	-1.216 ± 0.001	-0.735 ± 0.001	-1.186 ± 0.001	0.656 ± 0.001	0.860 ± 0.001
WISE J2344−3056	356.070739	−30.940633	-0.475 ± 0.001	0.281 ± 0.001	0.110 ± 0.001	0.632 ± 0.001	-0.235 ± 0.001	-0.376 ± 0.001	0.398 ± 0.001	-0.038 ± 0.001

[a]The relative positions of the image E are $\Delta\alpha = -0.330 \pm 0.003$ arcsec and $\Delta\delta = 0.326 \pm 0.002$ arcsec.

Only one of the quads in our sample, DES J0408−5354, has measured time delays: $\Delta t_{\rm AB}^{\rm observed} = -112 \pm 2.1$ d, $\Delta t_{\rm AD}^{\rm observed} = -155.5 \pm 12.8$ d (Courbin et al. 2018). The predicted time delays $\Delta t_{\rm AB}^{\rm predicted} = -100 \pm 9$ and $\Delta t_{\rm AD}^{\rm predicted} = -140 \pm 13$ d (Appendix C) are in good agreement with the measured values, although the measured values were not used as constraints in the modelling procedure.

In order to make the problem computationally tractable for much larger samples, we made some simplifying assumptions. Thus, whereas some of the lensing quantities, such as Einstein radius, deflector centre of mass, position angle and ellipticity, and image flux ratios, are robustly determined, our models are not appropriate for all applications. In particular, science cases requiring high precision might require more sophisticated modelling for each individual lens system.

The main simplifying assumptions in our work are (1) we restricted our models to simple yet general profiles to describe the mass and light distributions and (2) we assume no colour gradient in the deflector and source fluxes. Thus, we use the same scalelengths and ellipticity in the deflector- and source-light profiles in different bands while fitting simultaneously. Some straightforward ways to further improve the lens modelling are to allow for colour dependence of the light distribution of the source and deflector, explicitly including mass distribution of more nearby companions or satellites, increasing the number of shapelets ($n_{\rm max}$), and consider composite mass models consisting of both stellar and dark matter components.

We illustrate the information content of this large sample of quads by investigating the alignment between the light and mass distributions in the deflector galaxies, and the distribution of so-called flux ratio anomalies. Our key results are as follows:

(i) The centres of the mass and light distributions match very well (the rms of the offsets is 0.04).

(ii) We find the correlation between the ellipticity of the mass and light distributions to be weak (Pearson correlation coefficient, $r = 0.2$).

(iii) The position angles of the major axes of the mass and light distributions are well-aligned within $\pm 11°$ for 9 out of 13 lenses.

(iv) Systems with high ($>30°$) misalignment angle between the light and mass also have large external shear ($\gamma_{\rm ext} \gtrsim 0.1$). The Pearson correlation coefficient between the misalignment angle and the external shear is $r = 0.74$.

(v) The measured flux ratios between the images depart significantly from those predicted by our simple mass models. These flux ratio anomalies are strongest in the bluest band, consistent with microlensing being the main physical driver, in addition to millilensing associated with unseen satellites.

Our finding of weak correlation between the light and mass ellipticity slightly agrees with Keeton et al. (1998), Ferreras et al. (2008) and Rusu et al. (2016) who find no correlation. However, we do not find a strong correlation as Sluse et al. (2012) and Gavazzi et al. (2012) report. The weak correlation between the mass and light ellipticity in our study is consistent with the hierarchical formation scenario of elliptical galaxies, where the remnants in the simulation of multiple mergers are shown to have no correlation between the halo and light ellipticity (Weil & Hernquist 1996). Moreover, some of the deflectors in our sample are discy galaxies. The projected ellipticity of discy galaxies will not be correlated with the halo ellipticity if viewed from arbitrary orientations.

Moreover, dark matter haloes are expected to be rounder than the stellar distribution from simulation (Dubinski & Carlberg 1991;

Table 5. Photometry of the deflector and quasar images. The deflector magnitudes are calculated from the total flux within a 5 arcsec × 5 arcsec square aperture. Magnitudes are given in the AB system. The reported uncertainties are systematic and statistical uncertainties added in quadrature.

System name	Filter	Deflector	A	B	C	D
PS J0147+4630	F160W	18.3 ± 0.1	15.46 ± 0.03	15.78 ± 0.03	16.18 ± 0.03	18.05 ± 0.03
	F814W	19.4 ± 0.1	15.79 ± 0.03	16.09 ± 0.03	16.45 ± 0.03	18.21 ± 0.03
	F475X	21.8 ± 0.3	16.39 ± 0.03	16.67 ± 0.03	17.13 ± 0.03	18.74 ± 0.03
SDSS J0248+1913	F160W	20.8 ± 0.1	19.88 ± 0.04	20.41 ± 0.04	19.91 ± 0.03	20.13 ± 0.04
	F814W	22.7 ± 0.1	20.20 ± 0.03	20.23 ± 0.03	20.43 ± 0.03	20.66 ± 0.03
	F475X	26.4 ± 0.3	21.14 ± 0.03	21.18 ± 0.03	21.35 ± 0.03	21.80 ± 0.03
ATLAS J0259−1635	F160W	20.7 ± 0.1	18.48 ± 0.03	18.57 ± 0.04	19.06 ± 0.03	19.30 ± 0.04
	F814W	22.7 ± 0.1	19.00 ± 0.03	19.16 ± 0.03	19.62 ± 0.03	19.70 ± 0.03
	F475X	−	21.08 ± 0.03	20.81 ± 0.03	21.50 ± 0.04	21.33 ± 0.03
DES J0405−3308	F160W	20.2 ± 0.1	19.43 ± 0.07	19.58 ± 0.04	19.60 ± 0.04	19.33 ± 0.03
	F814W	22.0 ± 0.1	20.22 ± 0.04	20.60 ± 0.04	20.33 ± 0.03	20.09 ± 0.03
	F475X	25.0 ± 0.3	22.16 ± 0.04	22.81 ± 0.04	22.04 ± 0.03	21.91 ± 0.03
DES J0408−5354	F160W	18.6 ± 0.1	20.18 ± 0.03	19.79 ± 0.04	20.33 ± 0.04	20.82 ± 0.04
	F814W	19.9 ± 0.1	20.38 ± 0.03	20.00 ± 0.03	21.66 ± 0.03	20.87 ± 0.03
	F475X	22.6 ± 0.3	21.20 ± 0.03	21.34 ± 0.03	23.16 ± 0.03	21.86 ± 0.04
DES J0420−4037	F160W	18.6 ± 0.1	20.18 ± 0.03	21.03 ± 0.04	21.85 ± 0.04	21.96 ± 0.05
	F814W	19.5 ± 0.1	20.44 ± 0.03	20.96 ± 0.03	21.71 ± 0.03	21.98 ± 0.04
	F475X	21.5 ± 0.3	20.66 ± 0.03	21.25 ± 0.03	22.09 ± 0.03	22.09 ± 0.03
PS J0630−1201[a]	F160W	20.4 ± 0.1	18.71 ± 0.03	18.82 ± 0.03	18.74 ± 0.03	21.01 ± 0.04
	F814W	22.5 ± 0.1	19.70 ± 0.03	19.67 ± 0.03	19.71 ± 0.03	21.67 ± 0.03
	F475X	26.7 ± 0.3	21.06 ± 0.03	20.92 ± 0.03	21.10 ± 0.03	23.03 ± 0.03
SDSS J1251+2935	F160W	18.3 ± 0.1	19.35 ± 0.03	20.25 ± 0.05	21.30 ± 0.06	21.02 ± 0.05
	F814W	19.4 ± 0.1	20.01 ± 0.03	20.80 ± 0.04	22.80 ± 0.06	21.66 ± 0.04
	F475X	21.4 ± 0.3	20.01 ± 0.03	20.73 ± 0.04	22.73 ± 0.04	21.95 ± 0.04
SDSS J1330+1810	F160W	17.9 ± 0.1	19.17 ± 0.03	19.36 ± 0.03	20.00 ± 0.03	21.24 ± 0.05
	F814W	19.1 ± 0.1	20.11 ± 0.03	20.03 ± 0.03	20.48 ± 0.03	20.56 ± 0.03
	F475X	21.4 ± 0.3	20.31 ± 0.03	20.82 ± 0.04	21.24 ± 0.03	21.58 ± 0.04
SDSS J1433+6007	F160W	18.1 ± 0.1	20.43 ± 0.03	20.47 ± 0.04	20.55 ± 0.04	21.56 ± 0.04
	F814W	19.2 ± 0.1	20.25 ± 0.03	20.17 ± 0.03	20.45 ± 0.03	21.74 ± 0.03
	F475X	21.2 ± 0.3	20.31 ± 0.03	20.16 ± 0.03	20.49 ± 0.03	21.93 ± 0.04
PS J1606−2333	F160W	19.5 ± 0.1	19.59 ± 0.03	19.65 ± 0.04	19.99 ± 0.03	19.47 ± 0.03
	F814W	20.6 ± 0.1	19.06 ± 0.03	19.22 ± 0.03	19.38 ± 0.03	19.52 ± 0.03
	F475X	21.8 ± 0.3	19.52 ± 0.04	19.76 ± 0.04	19.97 ± 0.03	20.48 ± 0.04
DES J2038−4008	F160W	16.4 ± 0.1	18.48 ± 0.03	18.27 ± 0.03	18.60 ± 0.03	19.49 ± 0.04
	F814W	17.4 ± 0.1	20.25 ± 0.03	19.99 ± 0.03	20.05 ± 0.03	20.88 ± 0.03
	F475X	19.1 ± 0.3	21.02 ± 0.03	20.89 ± 0.03	20.71 ± 0.03	21.43 ± 0.03
WISE J2344−3056	F160W	19.0 ± 0.1	21.36 ± 0.05	20.94 ± 0.04	21.16 ± 0.06	20.78 ± 0.04
	F814W	20.0 ± 0.1	21.76 ± 0.03	21.20 ± 0.03	21.27 ± 0.03	20.76 ± 0.03
	F475X	21.6 ± 0.3	22.79 ± 0.03	21.68 ± 0.03	21.66 ± 0.03	21.13 ± 0.03

[a]The magnitudes of image E are 22.51 ± 0.10, $23.40 \pm .04$, and 24.77 ± 0.04 in the F160W, F814W, and F475X bands, respectively.

Warren et al. 1992; Dubinski 1994) with reported agreements to observations (Bruderer et al. 2016; Rusu et al. 2016). In our sample, the majority of the systems follow this prediction. Only three systems have significantly flatter mass distribution than the light distribution (DES J0408−5354, PS J0630−1201, and WISE J2344−3056). All these systems have satellites or comparable-mass companions and thus are not the typically relaxed systems where we expect this to hold. In contrast, four systems in our sample are significantly rounder in mass than in light: ATLAS J0259−1635, DES J0405−3308, DES J0420−4037, and PS J1606−2333. These are likely to be discy galaxies from visual inspection of their shapes. This explains the large difference in ellipticity between the mass and light.

To reliably compare the ellipticity of the light and mass distribution, the ellipticity needs to be estimated within the same aperture, or within an aperture large enough beyond that the ellipticity does not significantly evolve. From a strong-lens system, only the total (projected) mass within the Einstein radius can be estimated. If the Einstein radius is much smaller than the effective radius of the deflector galaxy, the comparison of ellipticity between light and mass may not be representative of the entire galaxy.

We find a strong alignment between the mass and light position angles, which agree very well with previous reports (Kochanek 2002; Ferreras et al. 2008; Treu et al. 2009; Gavazzi et al. 2012; Sluse et al. 2012; Bruderer et al. 2016). Our result is also in agreement with Bruderer et al. (2016) that the systems with high misalignment (>30°) also have strong external shear ($\gamma_{\text{ext}} \gtrsim 0.1$). The absence of systems with high misalignment but low external shear is in agreement with the prediction of galaxy formation models. Orbits that are highly misaligned in isolated galaxies (thus with low external shear) are shown to be rare and unstable (Heiligman & Schwarzschild 1979; Martinet & de Zeeuw 1988; Adams et al. 2007; Debattista et al. 2015). The misalignment in
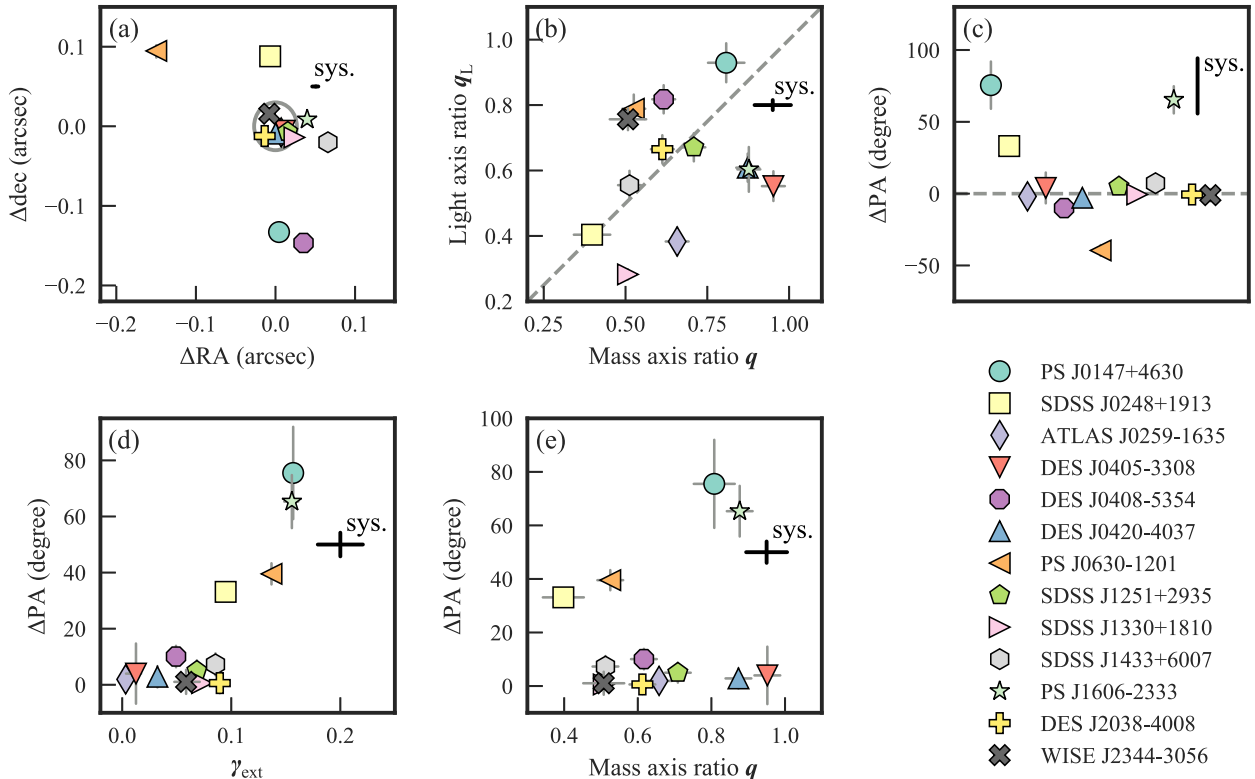
Figure 5. Mass and light alignments in the deflector galaxies: comparison between (a) the mass and light centroids, (b) the axis ratios of the light and mass profiles, (c) the misalignment angle (between the mass and light profiles' position angles), (d) the misalignment angle and the external shear, and (e) the misalignment angle and the mass profile axial ratio. The thin-solid-grey lines attached to the data points show 1σ statistical uncertainty and the thick-solid-black bars annotated with 'sys.' in each figure shows the 1σ systematic uncertainty. The systematic uncertainty is estimated by marginalizing over various numerical settings for the system SDSS J0248+1913 as described in Section 3.4. In (a) the solid-grey ellipse centred at (0, 0) shows the root-mean-square (rms) spread of ΔRA and ΔDec. for nine lens systems excluding the systems with large deviations: PS J0147+4630, DES J0408−5354, and PS J0630−1201. This rms spread can be taken as the upper limit of the systematics. The dashed grey line traces the perfect 1-to-1 correlation in (b) and the zero misalignment in (c) to aid visualisation. The centres of the mass and light distributions match very well (a). The systems with large offsets between the mass and light centroids have satellites or comparable-mass companions possibly biasing the centroid estimate. The axis ratios of the light and mass distributions are only weakly correlated (b). The position angles align very well within $\pm12°$ for 8 out of the 12 systems (c). Systems with large misalignment have larger values of external shear (d). However, there is very weak to no correlation between the position angle misalignment and mass ellipticity (e).

isolated galaxies can only be sustained by a constant gas-inflow in blue starburst galaxies (Debattista et al. 2015).

Furthermore, for systems with $\theta_E/\theta_{eff} < 1$, the lensing mass is likely to be dominated by the stellar mass. In that case, relatively stronger correlation between the mass and the light distributions is naturally expected. A comparison between the dark matter and luminous matter distribution would be more interesting in regard to directly testing ΛCDM and galaxy formation theories. However, broadly speaking, large deviations in ellipticity and alignment in our sample have to be explained by the presence of dark matter. However, direct comparison between the dark and luminous mass distributions requires composite mass models with dark and luminous components as adopted by Bruderer et al. (2016). Gomer & Williams (2018) find that two elliptical mass distributions corresponding to the dark matter and baryon with an offset can better reproduce the image positions in quads than just one smooth elliptical mass distribution with external shear. Those kinds of mass models are beyond the scope of this paper and left for future studies.

The departures of flux-ratios from the smooth model in the discy galaxies in our sample are not at the extreme of the χ_f^2-distribution.

This further supports microlensing by foreground stars being the dominant source of the flux-ratio anomaly.

Detailed follow-up of this sample is under way, to measure redshift and velocity dispersion of the deflectors as well as the time delays between the quasars and the properties of the environment. Once follow-up is completed, we will use this sample to address fundamental questions such as the determination of the Hubble Constant (e.g. Bonvin et al. 2017), the nature of dark matter (e.g. Gilman et al. 2018), and the normalization of the stellar IMF in massive galaxies (e.g. Schechter et al. 2014).
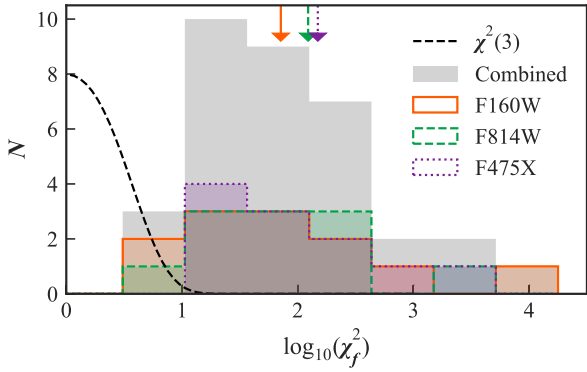
Figure 6. Distribution of χ_f^2 for flux-ratio anomalies from Equation (4) assuming 20 per cent error in flux. The distribution is for 12 quads in our sample excluding PS J0630−1201. The χ_f^2-distributions in bands F160W, F814W, and F475X are shown in orange, green, and purple shaded regions, respectively. The χ_f^2-distribution from all the bands combined is shown as the grey shaded region. The black dashed line shows the expected $\chi_f^2 \sim \chi^2(3)$ distribution in the absence of microlensing. The arrows on the top show the mean of the χ_f^2-values in bands F160W (solid orange), F814W (dashed green), and F475X (dotted purple). The combined χ_f^2-distribution is shifted to higher values. The shift is higher for shorter wavelengths, as the quasar size gets smaller with decreasing wavelength making it more susceptible to microlensing.

REFERENCES

Adams F. C., Bloch A. M., Butler S. C., Druce J. M., Ketchum J. A., 2007, ApJ, 670, 1027

Agnello A., Grillo C., Jones T., Treu T., Bonamigo M., Suyu S. H., 2018a, MNRAS, 474, 3391

Agnello A., Kelly B. C., Treu T., Marshall P. J., 2015, MNRAS, 448, 1446

Agnello A. et al., 2017, MNRAS, 472, 4038

Agnello A. et al., 2018b, MNRAS, 475, 2086

Agnello A. et al., 2018c, MNRAS, 479, 4345
Akeret J., Seehars S., Amara A., Refregier A., Csillaghy A., 2013, Astron. Comp., 2, 27
Amara A., Metcalf R. B., Cox T. J., Ostriker J. P., 2006, MNRAS, 367, 1367
Anguita T., Faure C., Yonehara A., Wambsganss J., Kneib J.-P., Covone G., Alloin D., 2008, A&A, 481, 615
Anguita T. et al., 2018, MNRAS, 480, 5017
Astropy Collaboration et al., 2013, A&A, 558, A33
Auger M. W., Treu T., Bolton A. S., Gavazzi R., Koopmans L. V. E., Marshall P. J., Moustakas L. A., Burles S., 2010b, ApJ, 724, 511
Auger M. W., Treu T., Gavazzi R., Bolton A. S., Koopmans L. V. E., Marshall P. J., 2010a, ApJ, 721, L163
Berghea C. T., Nelson G. J., Rusu C. E., Keeton C. R., Dudik R. P., 2017, ApJ, 844, 90
Bernal J. L., Verde L., Riess A. G., 2016, J. Cosmol. Astropart. Phys., 10, 019
Birrer S. et al., 2019, MNRAS, preprint (arXiv:1809.01274)
Birrer S., Amara A., 2018, Astrophysics Source Code Library, record, ascl:1804.012
Birrer S., Amara A., Refregier A., 2015, ApJ, 813, 102
Birrer S., Amara A., Refregier A., 2016, J. Cosmol. Astropart. Phys., 8, 020
Birrer S., Amara A., Refregier A., 2017, J. Cosmol. Astropart. Phys., 5, 037
Bonvin V. et al., 2017, MNRAS, 465, 4914
Boylan-Kolchin M., Bullock J. S., Kaplinghat M., 2011, MNRAS, 415, L40
Bruderer C., Read J. I., Coles J. P., Leier D., Falco E. E., Ferreras I., Saha P., 2016, MNRAS, 456, 870
Cappellari M. et al., 2012, Nature, 484, 485
Chen G. C.-F. et al., 2016, MNRAS, 462, 3457
Claeskens J.-F., Sluse D., Riaud P., Surdej J., 2006, A&A, 451, 865
Collett T. E., 2015, ApJ, 811, 20
Courbin F. et al., 2018, A&A, 609, A71
Dalal N., Kochanek C. S., 2002, ApJ, 572, 25
Dawson K. S. et al., 2013, AJ, 145, 10
Debattista V. P., Moore B., Quinn T., Kazantzidis S., Maas R., Mayer L., Read J., Stadel J., 2008, ApJ, 681, 1076
Debattista V. P., van den Bosch F. C., Roškar R., Quinn T., Moore B., Cole D. R., 2015, MNRAS, 452, 4094
Delchambre L. et al., 2018, preprint (arXiv:1807.02845)
Diehl H. T. et al., 2017, ApJS, 232, 15
Dubinski J., 1994, ApJ, 431, 617
Dubinski J., Carlberg R. G., 1991, ApJ, 378, 496
D'Souza R., Kauffman G., Wang J., Vegetti S., 2014, MNRAS, 443, 1433
Ene I. et al., 2018, MNRAS, 479, 2810
Ferreras I., Saha P., Burles S., 2008, MNRAS, 383, 857
Foreman-Mackey D., Hogg D. W., Lang D., Goodman J., 2013, PASP, 125, 306
Gavazzi R., Treu T., Marshall P. J., Brault F., Ruff A., 2012, ApJ, 761, 170
Gilman D., Agnello A., Treu T., Keeton C. R., Nierenberg A. M., 2017, MNRAS, 467, 3970
Gilman D., Birrer S., Treu T., Keeton C. R., Nierenberg A., 2018, MNRAS, 481, 819
Gomer M. R., Williams L. L. R., 2018, MNRAS, 475, 1987
Goodman J., Weare J., 2010, Commun. Appl. Math. Comput. Sci., 5, 65
Goullaud C. F., Jensen J. B., Blakeslee J. P., Ma C.-P., Greene J. E., Thomas J., 2018, ApJ, 856, 11
Heiligman G., Schwarzschild M., 1979, ApJ, 233, 872
Hezaveh Y. D., Levasseur L. P., Marshall P. J., 2017, Nature, 548, 555
Hezaveh Y. D. et al., 2016, ApJ, 823, 37
Hsueh J.-W., Fassnacht C. D., Vegetti S., McKean J. P., Spingola C., Auger M. W., Koopmans L. V. E., Lagattuta D. J., 2016, MNRAS, 463, L51
Hsueh J.-W. et al., 2017, MNRAS, 469, 3713
Hunter J. D., 2007, Comput. Sci. Eng., 9, 90
Ibata R., Lewis G. F., Irwin M., Totten E., Quinn T., 2001, ApJ, 551, 294
Inada N. et al., 2012, AJ, 143, 119
Jedrzejewski R. I., 1987, MNRAS, 226, 747
Jee I., Komatsu E., Suyu S. H., Huterer D., 2016, J. Cosmol. Astropart. Phys., 4, 031
Jing Y. P., Suto Y., 2002, ApJ, 574, 538

Jones E., Oliphant T., Peterson P., Others, 2001, SciPy: Open Source Scientific Tools for Python, http://www.scipy.org/
Katz N., Gunn J. E., 1991, ApJ, 377, 365
Kauffmann G., White S. D. M., Guiderdoni B., 1993, MNRAS, 264, 201
Kayo I. et al., 2007, AJ, 134, 1515
Kazantzidis S., Kravtsov A. V., Zentner A. R., Allgood B., Nagai D., Moore B., 2004, ApJ, 611, L73
Keeton C. R., Kochanek C. S., Falco E. E., 1998, ApJ, 509, 561
Keeton C. R., Moustakas L. A., 2009, ApJ, 699, 1720
Kluyver T. et al., 2016, in Loizides F., Schmidt B., eds, Positioning and Power in Academic Publishing: Players, Agents and Agendas. p. 87
Klypin A., Kravtsov A. V., Valenzuela O., Prada F., 1999, ApJ, 522, 82
Kochanek C. S., 2002, in Natarajan P., ed., The Shapes of Galaxies and Their Dark Halos. World Scientific, Singapore, p. 62
Kochanek C. S., Dalal N., 2004, ApJ, 610, 69
Koopmans L. V. E., 2005, MNRAS, 363, 1136
Lackner C. N., Gunn J. E., 2012, MNRAS, 421, 2277
Lee C.-H., 2017, A&A, 605, L8
Lee C.-H., 2018, MNRAS, 475, 3086
Lemon C. A., Auger M. W., McMahon R. G., Ostrovski F., 2018, MNRAS, 479, 5060
Linder E. V., 2011, Phys. Rev. D, 84, 123529
Lin H. et al., 2017, ApJ, 838, L15
Lux H., Read J. I., Lake G., Johnston K. V., 2012, MNRAS, 424, L16
Macciò A. V., Dutton A. A., van den Bosch F. C., Moore B., Potter D., Stadel J., 2007, MNRAS, 378, 55
Martinet L., de Zeeuw T., 1988, A&A, 206, 269
Metcalf R. B., Amara A., 2012, MNRAS, 419, 3414
Metcalf R. B., Madau P., 2001, ApJ, 563, 9
Metcalf R. B., Zhao H., 2002, ApJ, 567, L5
Moore B., Quinn T., Governato F., Stadel J., Lake G., 1999, MNRAS, 310, 1147
Moustakas L. A. et al., 2009, Astro2010: The Astronomy and Astrophysics Decadal Survey, Science White Papers, no. 214
Navarro J. F., Frenk C. S., White S. D. M., 1996, ApJ, 462, 563
Nierenberg A. M., Treu T., Wright S. A., Fassnacht C. D., Auger M. W., 2014, MNRAS, 442, 2434
Nierenberg A. M. et al., 2017, MNRAS, 471, 2224
Nightingale J., Dye S., Massey R., 2018, MNRAS, 478, 4738
Oguri M., Inada N., Blackburne J. A., Shin M.-S., Kayo I., Strauss M. A., Schneider D. P., York D. G., 2008, MNRAS, 391, 1973
Oguri M., Marshall P. J., 2010, MNRAS, 405, 2579
Oguri M., Rusu C. E., Falco E. E., 2014, MNRAS, 439, 2494
Oguri M. et al., 2006, AJ, 132, 999
Oh S., Greene J. E., Lackner C. N., 2017, ApJ, 836, 115
Oliphant T. E., 2015, Guide to NumPy, 2nd edn. Public Domain, (https://archive.org/details/NumPyBook)
Ostrovski F. et al., 2017, MNRAS, 465, 4325
Ostrovski F. et al., 2018, MNRAS, 473, L116
Perreault Levasseur L., Hezaveh Y. D., Wechsler R. H., 2017, ApJ, 850, L7
Planck Collaboration VI, 2018, preprint (arXiv:1807.06209)
Read J. I., 2014, J. Phys. G: Nucl. Phys., 41, 063101
Refregier A., 2003, MNRAS, 338, 35
Refsdal S., 1964, MNRAS, 128, 307
Riess A. G. et al., 2016, ApJ, 826, 56
Riess A. G. et al., 2018a, ApJ, 855, 136
Riess A. G. et al., 2018b, ApJ, 861, 126
Romanowsky A. J., Kochanek C. S., 1998, ApJ, 493, 641
Rusu C. E. et al., 2016, MNRAS, 458, 2
Rusu C. E. et al., 2017, MNRAS, 467, 4220
Schechter P. L., Anguita T., Morgan N. D., Read M., Shanks T., 2018, Res. Notes AAS, 2, 21
Schechter P. L., Morgan N. D., Chehade B., Metcalfe N., Shanks T., McDonald M., 2017, AJ, 153, 219
Schechter P. L., Pooley D., Blackburne J. A., Wambsganss J., 2014, ApJ, 793, 96

Schneider P., Kochanek C. S., Wambsganss J., 2006, Gravitational Lensing: Strong, Weak and Micro. Saas-Fee Advanced Courses, Vol. 33. Springer, Berlin

Shajib A. J., Treu T., Agnello A., 2018, MNRAS, 473, 210

Shajib A. J., Wright E. L., 2016, ApJ, 827, 116

Sluse D., Chantry V., Magain P., Courbin F., Meylan G., 2012, A&A, 538, A99

Sluse D. et al., 2017, MNRAS, 470, 4838

Sonnenfeld A. et al., 2018, PASJ, 70, S29

Stoughton C. et al., 2002, AJ, 123, 485

Suyu S. H., Marshall P. J., Auger M. W., Hilbert S., Blandford R. D., Koopmans L. V. E., Fassnacht C. D., Treu T., 2010, ApJ, 711, 201

Suyu S. H. et al., 2012, preprint (arXiv:1202.4459)

Suyu S. H. et al., 2013, ApJ, 766, 70

Suyu S. H. et al., 2017, MNRAS, 468, 2590

Sérsic J. L., 1968, Atlas de Galaxias Australes. Observatorio Astronomico, Cordoba, Argentina

Tihhonova O. et al., 2018, MNRAS, 477, 5657

Treu T., 2010, ARA&A, 48, 87

Treu T., Auger M. W., Koopmans L. V. E., Gavazzi R., Marshall P. J., Bolton A. S., 2010, ApJ, 709, 1195

Treu T., Gavazzi R., Gorecki A., Marshall P. J., Koopmans L. V. E., Bolton A. S., Moustakas L. A., Burles S., 2009, ApJ, 690, 670

Treu T., Marshall P. J., 2016, Astron. Astrophys. Rev., 24, 11

Treu T. et al., 2018, MNRAS, 481, 1041

van Dokkum P. G., Conroy C., 2010, Nature, 468, 940

Vegetti S., Despali G., Lovell M. R., Enzi W., 2018, MNRAS, 481, 3661

Vegetti S., Koopmans L. V. E., 2009, MNRAS, 392, 945

Vegetti S., Koopmans L. V. E., Bolton A., Treu T., Gavazzi R., 2010, MNRAS, 408, 1969

Vegetti S., Lagattuta D. J., McKean J. P., Auger M. W., Fassnacht C. D., Koopmans L. V. E., 2012, Nature, 481, 341

Viel M., Becker G. D., Bolton J. S., Haehnelt M. G., 2013, Phys. Rev. D, 88, 043502

Warren M. S., Quinn P. J., Salmon J. K., Zurek W. H., 1992, ApJ, 399, 405

Weil M. L., Hernquist L., 1996, ApJ, 460, 101

Weinberg D. H., Mortonson M. J., Eisenstein D. J., Hirata C., Riess A. G., Rozo E., 2013, Phys. Rep., 530, 87

Williams P., Agnello A., Treu T., 2017, MNRAS, 466, 3088

Williams P. R. et al., 2018, MNRAS, 477, L70

Witt H. J., Mao S., Schechter P. L., 1995, ApJ, 443, 18

Wong K. C. et al., 2017, MNRAS, 465, 4895

Xu D., Sluse D., Gao L., Wang J., Frenk C., Mao S., Schneider P., Springel V., 2015, MNRAS, 447, 3189

Yonehara A., Hirashita H., Richter P., 2008, A&A, 478, 95

Yoo J., Kochanek C. S., Falco E. E., McLeod B. A., 2006, ApJ, 642, 22

APPENDIX A: LENS LIGHT PARAMETERS

We report the parameters of the best-fitting Sérsic functions for the deflectors in Table A1.

Table A1. Lens light parameters. The reported uncertainties are systematic and statistical uncertainties added in quadrature. The magnitudes are given in AB system.

System name	n_{Sersic}	θ_{eff} (arcsec)	I_e (F160W) (mag arcsec^{-2})	I_e (F814W) (mag arcsec^{-2})	I_e (F475X) (mag arcsec^{-2})	q_L	ϕ_L (E of N) (deg)
PS J0147+4630	4	4.97 ± 0.03	29.7 ± 1.0	32.2 ± 1.0	34.4 ± 1.5	0.81 ± 0.01	18 ± 1
	1	0.14 ± 0.03	23.4 ± 0.9	26.7 ± 0.9	30.0 ± 1.3	0.87 ± 0.01	62 ± 1
SDSS J0248+1913	2.4 ± 1.4	0.16 ± 0.03	24.5 ± 0.4	27.8 ± 0.4	31.6 ± 0.6	0.40 ± 0.02	13 ± 1
ATLAS J0259−1635	11.8 ± 1.4	1.00 ± 0.03	28.7 ± 1.0	32.2 ± 1.0	−	0.38 ± 0.02	20 ± 1
DES J0405−3308	7.6 ± 1.4	0.44 ± 0.03	26.8 ± 1.0	30.1 ± 1.0	33.1 ± 1.5	0.55 ± 0.02	37 ± 1
DES J0408−5354	5.5 ± 1.4	2.15 ± 0.03	28.5 ± 1.0	31.3 ± 1.0	34.0 ± 1.5	0.82 ± 0.01	28 ± 2
DES J0420−4037	4.0 ± 1.4	0.44 ± 0.03	25.1 ± 1.0	27.5 ± 1.0	29.5 ± 1.5	0.61 ± 0.01	27 ± 1
PS J0630−1201	6.8 ± 1.4	1.64 ± 0.03	29.9 ± 1.0	33.5 ± 1.0	37.7 ± 1.5	0.79 ± 0.01	12 ± 1
SDSS J1251+2935	4	0.53 ± 0.03	25.5 ± 1.0	28.1 ± 1.0	30.4 ± 1.5	0.67 ± 0.01	23 ± 1
	1	5.00 ± 0.03	30.4 ± 0.9	32.6 ± 0.9	34.0 ± 1.3	0.67 ± 0.03	16 ± 3
SDSS J1330+1810	4	0.75 ± 0.03	24.8 ± 0.4	27.7 ± 0.4	31.9 ± 0.6	0.26 ± 0.01	24 ± 1
	1	0.37 ± 0.03	24.5 ± 0.4	26.7 ± 0.4	27.9 ± 0.6	0.37 ± 0.01	25 ± 1
SDSS J1433+6007	4	0.56 ± 0.03	25.4 ± 1.0	28.2 ± 1.0	30.4 ± 1.5	0.56 ± 0.02	-88 ± 2
	1	3.35 ± 0.03	28.9 ± 0.9	31.1 ± 0.9	32.8 ± 1.3	0.54 ± 0.02	-88 ± 1
PS J1606−2333	4	0.11 ± 0.03	25.2 ± 1.0	27.7 ± 1.0	−	0.56 ± 0.06	-26 ± 4
	1	1.66 ± 0.04	28.5 ± 0.9	31.0 ± 0.9	32.1 ± 1.3	0.77 ± 0.02	-11 ± 2
DES J2038−4008	4	3.36 ± 0.03	26.7 ± 1.0	29.3 ± 1.0	31.1 ± 1.5	0.64 ± 0.01	38 ± 1
	1	4.99 ± 0.03	29.2 ± 0.9	31.3 ± 0.9	32.6 ± 1.3	0.47 ± 0.01	-62 ± 1
WISE J2344−3056	4	0.61 ± 0.04	26.9 ± 1.0	30.9 ± 1.0	−	0.75 ± 0.03	-68 ± 4
	1	4.67 ± 0.05	30.1 ± 0.9	31.7 ± 0.9	33.1 ± 1.3	0.80 ± 0.07	65 ± 10

APPENDIX B: CONVERGENCE, SHEAR, AND STELLAR CONVERGENCE

The convergence κ, shear γ, and the stellar convergence $\kappa_\star$ at the image positions for each lens are given in Table B1. The convergence at the image position is given by the lens mass

Table B1. Convergence, shear, and stellar convergence at the image positions. The reported uncertainties are systematic and statistical uncertainties added in quadrature. The stellar convergence, $\kappa_\star$, is estimated from the F160W band for the lenses with double Sérsic fit for the lens light.

System name	Image	κ	γ	$\kappa_\star/\kappa$
PS J0147+4630	A	0.41 ± 0.03	0.55 ± 0.04	0.37 ± 0.17
	B	0.39 ± 0.03	0.52 ± 0.04	0.37 ± 0.17
	C	0.43 ± 0.03	0.45 ± 0.03	0.27 ± 0.12
	D	0.84 ± 0.06	0.99 ± 0.08	0.41 ± 0.18
SDSS J0248+1913	A	0.63 ± 0.05	0.87 ± 0.06	0.002 ± 0.001
	B	0.26 ± 0.03	0.50 ± 0.02	0.003 ± 0.002
	C	0.20 ± 0.03	0.31 ± 0.02	0.006 ± 0.003
	D	0.87 ± 0.07	1.04 ± 0.09	0.011 ± 0.003
ATLAS J0259−1635	A	0.41 ± 0.03	0.42 ± 0.03	0.06 ± 0.03
	B	0.66 ± 0.05	0.67 ± 0.05	0.25 ± 0.15
	C	0.36 ± 0.03	0.36 ± 0.02	0.05 ± 0.03
	D	0.64 ± 0.04	0.65 ± 0.04	0.21 ± 0.11
DES J0405−3308	A	0.48 ± 0.04	0.46 ± 0.03	0.06 ± 0.02
	B	0.53 ± 0.04	0.53 ± 0.04	0.20 ± 0.08
	C	0.52 ± 0.04	0.51 ± 0.04	0.19 ± 0.08
	D	0.49 ± 0.03	0.47 ± 0.03	0.06 ± 0.02
DES J0408−5354	A	0.34 ± 0.02	0.31 ± 0.02	0.17 ± 0.06
	B	0.45 ± 0.03	0.35 ± 0.02	0.24 ± 0.09
	C	0.57 ± 0.04	0.57 ± 0.04	0.17 ± 0.07
	D	0.75 ± 0.05	0.68 ± 0.05	0.32 ± 0.13
DES J0420−4037	A	0.56 ± 0.04	0.56 ± 0.04	0.12 ± 0.05
	B	0.50 ± 0.04	0.44 ± 0.03	0.07 ± 0.03
	C	0.45 ± 0.03	0.41 ± 0.03	0.05 ± 0.02
	D	0.56 ± 0.04	0.51 ± 0.04	0.16 ± 0.06
PS J0630−1201	A	0.52 ± 0.04	0.45 ± 0.03	0.07 ± 0.05
	B	0.49 ± 0.03	0.52 ± 0.04	0.07 ± 0.05
	C	0.45 ± 0.03	0.55 ± 0.04	0.07 ± 0.04
	D	1.39 ± 0.10	1.23 ± 0.08	0.03 ± 0.02
SDSS J1251+2935	A	0.57 ± 0.04	0.57 ± 0.04	0.21 ± 0.08
	B	0.50 ± 0.04	0.41 ± 0.03	0.17 ± 0.07
	C	0.63 ± 0.04	0.57 ± 0.04	0.21 ± 0.09
	D	0.33 ± 0.02	0.25 ± 0.02	0.12 ± 0.05
SDSS J1330+1810	A	0.48 ± 0.08	0.43 ± 0.04	0.04 ± 0.02
	B	0.59 ± 0.09	0.52 ± 0.05	0.16 ± 0.08
	C	0.36 ± 0.06	0.43 ± 0.04	0.02 ± 0.01
	D	0.74 ± 0.12	0.71 ± 0.06	0.23 ± 0.12
SDSS J1433+6007	A	0.35 ± 0.02	0.20 ± 0.01	0.08 ± 0.03
	B	0.38 ± 0.03	0.35 ± 0.02	0.10 ± 0.04
	C	0.78 ± 0.06	0.72 ± 0.05	0.16 ± 0.06
	D	1.20 ± 0.09	1.16 ± 0.08	0.22 ± 0.09
PS J1606−2333	A	0.46 ± 0.03	0.25 ± 0.02	0.50 ± 0.20
	B	0.49 ± 0.03	0.22 ± 0.02	0.53 ± 0.22
	C	0.77 ± 0.06	0.75 ± 0.05	0.61 ± 0.25
	D	0.57 ± 0.04	0.66 ± 0.05	0.77 ± 0.31
DES J2038−4008	A	0.21 ± 0.02	0.43 ± 0.03	0.73 ± 0.27
	B	0.22 ± 0.02	0.49 ± 0.03	0.73 ± 0.27
	C	0.45 ± 0.03	0.89 ± 0.06	0.72 ± 0.28
	D	0.59 ± 0.04	1.11 ± 0.08	0.74 ± 0.26
WISE J2344−3056	A	0.79 ± 0.06	0.69 ± 0.06	0.54 ± 0.22
	B	0.37 ± 0.03	0.38 ± 0.03	0.62 ± 0.25
	C	0.37 ± 0.03	0.38 ± 0.03	0.66 ± 0.26
	D	0.82 ± 0.07	0.72 ± 0.06	0.60 ± 0.24

distribution. We assume a constant mass-to-light ratio to convert the surface brightness distribution into a stellar surface mass-density distribution. We choose the maximum normalization factor for the stellar convergence that meets these two criteria: (i) the stellar convergence is smaller than the convergence and (ii) the integrated stellar convergence is smaller than two-thirds of the integrated convergence within half of the effective radius (Auger et al. 2010b).

APPENDIX C: TIME DELAYS

The time delay between two images I and J is given by

$$\Delta t_{\mathrm{IJ}} = \frac{D_{\Delta t}}{c}\left[\frac{1}{2}(\boldsymbol{\theta}_{\mathrm{I}} - \boldsymbol{\beta})^2 - \frac{1}{2}(\boldsymbol{\theta}_{\mathrm{J}} - \boldsymbol{\beta})^2 - \psi(\boldsymbol{\theta}_{\mathrm{I}}) + \psi(\boldsymbol{\theta}_{\mathrm{J}})\right], \quad \text{(C1)}$$

where $\boldsymbol{\theta}$ is the image position, $\boldsymbol{\beta}$ is the source position, ψ is the lensing potential, c is the speed of light, and $D_{\Delta t}$ is the time-delay distance given by

$$D_{\Delta t} = (1 + z_{\mathrm{d}})\frac{D_{\mathrm{d}}D_{\mathrm{s}}}{D_{\mathrm{ds}}}. \quad \text{(C2)}$$

Here, z_{d} is the deflector redshift, D_{d}, D_{s}, and D_{ds} are the angular diameter distances between the observer and the deflector, between the observer and the source, and between the deflector and the source, respectively. The predicted time delays between the images for the quads are given in Table C1.

Table C1. Predicted time-delays between the quasar images. The reported uncertainties are systematic and statistical uncertainties added in quadrature. We adopt fiducial redshifts $z_d = 0.5$ and $z_s = 2$, where the redshifts are not measured yet.

System name	z_d	z_s	Δt_{AB} (d)	Δt_{AC} (d)	Δt_{AD} (d)
PS J0147+4630	0.572	2.341	-2.1 ± 0.3	-7 ± 1	-193 ± 18
SDSS J0248+1913	0.5	2.0	2.7 ± 0.2	20 ± 2	-5.9 ± 0.4
ATLAS J0259−1635	0.5	2.16	-3.6 ± 0.3	7 ± 1	-2.7 ± 0.2
DES J0405−3308	0.5	1.713	-1.7 ± 0.2	-0.9 ± 0.2	-0.3 ± 0.2
DES J0408−5354	0.597	2.375	-100 ± 9	-105 ± 9	-140 ± 13
DES J0420−4037	0.5	2.0	1.8 ± 0.2	7 ± 1	1.4 ± 0.1
PS J0630−1201	0.5	3.34	-0.12 ± 0.02	-0.09 ± 0.02	-108 ± 10
SDSS J1251+2935	0.41	0.802	0.6 ± 0.1	-0.43 ± 0.04	36 ± 3
SDSS J1330+1810	0.373	1.393	-0.20 ± 0.02	6 ± 1	-11 ± 1
SDSS J1433+6007	0.407	2.737	-24 ± 2	-36 ± 3	-100 ± 9
PS J1606−2333	0.5	2.0	-3.8 ± 0.4	-11 ± 1	-7 ± 1
DES J2038−4008	0.23	0.777	-6 ± 1	-11 ± 1	-27 ± 2
WISE J2344−3056	0.5	2.0	3.3 ± 0.4	3.4 ± 0.4	-0.6 ± 0.2

APPENDIX D: LENS MODELS

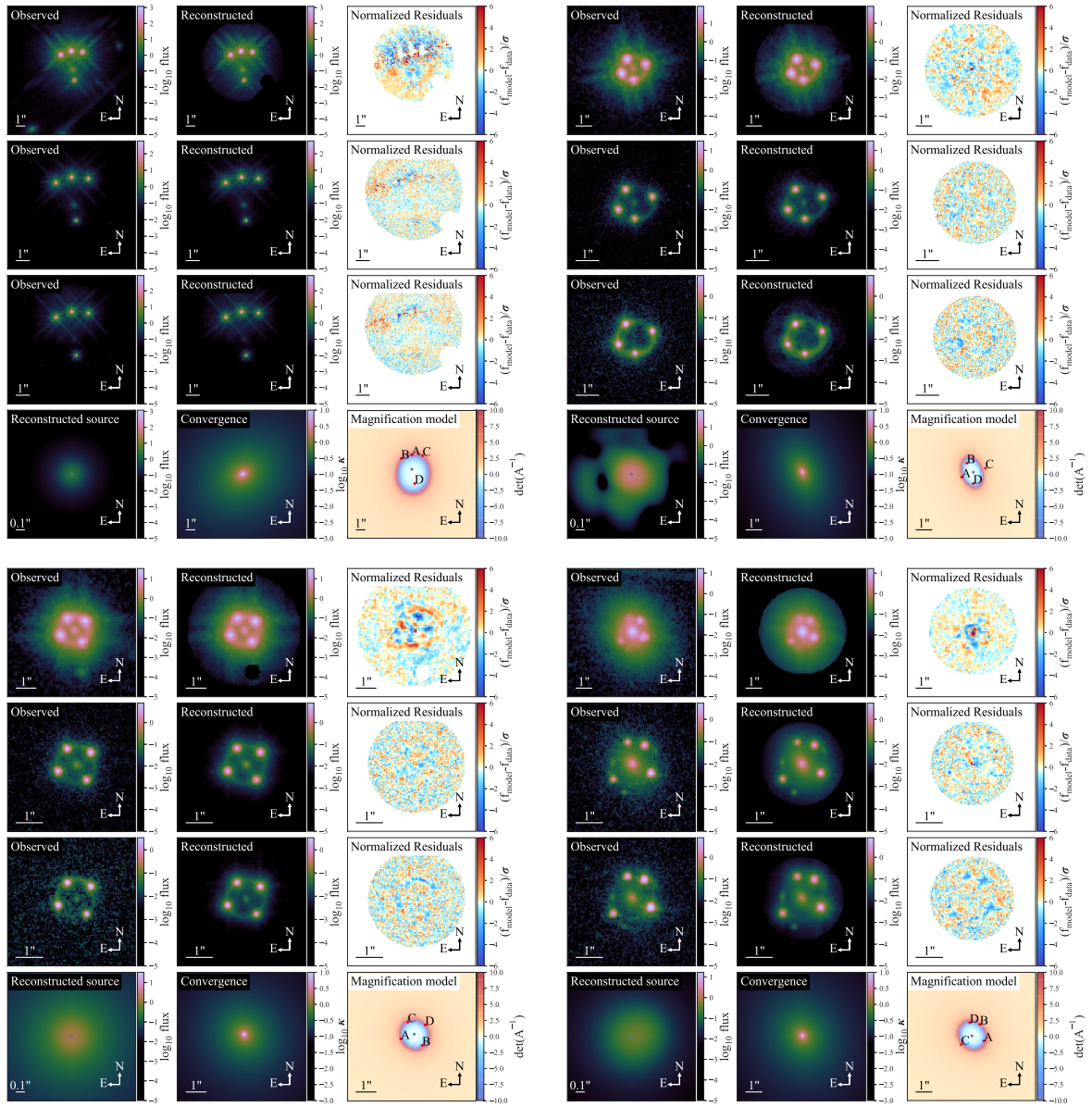In this section, we provide rest of the lens models in Figs D1–D3 that were not included in Fig. 3.

Figure D1. Best-fitting models for PS J0147+4630 (top left), ATLAS J0259−1635 (top right), DES J0405-3308 (bottom left), and DES J0420−4037 (bottom right). The first three rows for each lens system show the observed image, reconstructed lens image, and the normalized residuals in three *HST* bands: F160W, F814W, and F475X, respectively. The fourth row shows the reconstructed source in the F160W band, the convergence, and the magnification model.
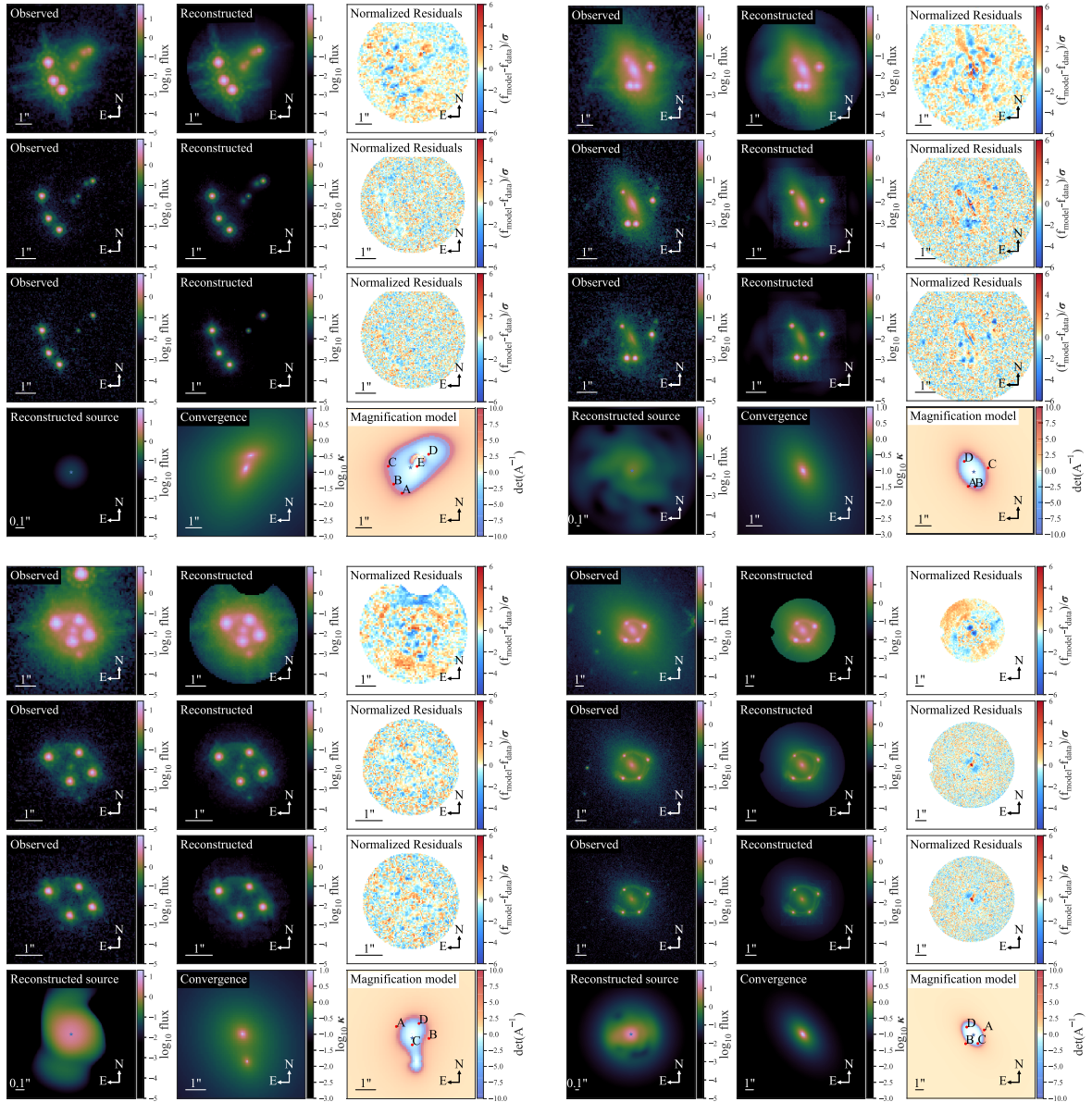
Figure D2. Best-fitting models for PS J0630−1201 (top left), SDSS J1330+1810 (top right), PS J1606−2333 (bottom left), and DES J2038−4008 (bottom right). The first three rows for each lens system show the observed image, reconstructed lens image, and the normalized residuals in three *HST* bands: F160W, F814W, and F475X, respectively. The fourth row shows the reconstructed source in the F160W band, the convergence, and the magnification model.

Figure D3. Best-fitting models for WISE J2344−3056. The first three rows show the observed image, reconstructed lens image, and the normalized residuals in three *HST* bands: F160W, F814W, and F475X, respectively. The fourth row shows the reconstructed source in the F160W band, the convergence, and the magnification model.
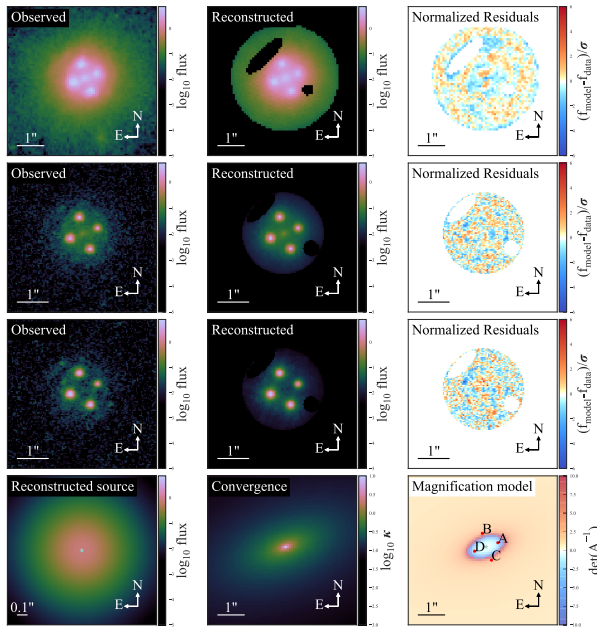
[1]*Department of Physics and Astronomy, University of California, Los Angeles, CA 90095, USA*

[2]*Institute of Astronomy, Madingley Road, Cambridge CB3 0HA, UK*

[3]*European Southern Observatory, Karl-Schwarzschild-Strasse 2, D-85748 Garching bei Muenchen, Germany*

[4]*Departamento de Ciencias Fisicas, Universidad Andres Bello Fernandez Concha 700, Las Condes, Santiago, Chile*

[5]*Millennium Institute of Astrophysics, Chile*

[6]*Fermi National Accelerator Laboratory, PO Box 500, Batavia, IL 60510, USA*

[7]*Institute of Physics, Laboratoire d'Astrophysique, Ecole Polytechnique Fédérale de Lausanne (EPFL), Observatoire de Sauverny, CH-1290 Versoix, Switzerland*

[8]*Institute of Cosmology and Gravitation, University of Portsmouth, Portsmouth PO1 3FX, UK*

[9]*Physics Dept. University of California, Davis, 1 Shields Ave., Davis, CA 95161, USA*

[10]*Kavli Institute for Cosmological Physics, The University of Chicago, Chicago, IL 60637, USA*

[11]*Department of Liberal Arts, Tokyo University of Technology, Ota-ku, Tokyo 144-8650, Japan*

[12]*Kavli Institute for Particle Astrophysics and Cosmology, PO Box 20450, MS29, Stanford, CA 94309, USA*

[13]*Kavli IPMU (WPI), UTIAS, The University of Tokyo, Kashiwa, Chiba 277-8583, Japan*

[14]*Staples High School, Westport, CT 06880, USA*

[15]*Instituto de Física y Astronomía, Universidad de Valparaíso, Avda. Gran Bretaña 1111, Playa Ancha, Valparaíso 2360102, Chile*

[16]*Research Center for the Early Universe, The University of Tokyo, 7-3-1 Hongo, Bunkyo-ku, Tokyo, 113-0033, Japan*

[17]*Department of Physics, The University of Tokyo, 7-3-1 Hongo, Bunkyo-ku, Tokyo 113-0033, Japan*

[18]*Kavli Institute for the Physics and Mathematics of the Universe (WPI), The University of Tokyo, 5-1-5 Kashiwanoha, Kashiwa, Chiba 277-8583, Japan*

[19]*Subaru telescope, National Astronomical Observatory of Japan, 650 North Aohoku Place, Hilo, HI 96720, USA*

[20]*MIT Kavli Institute for Astrophysics and Space Research, Cambridge, MA 02139, USA*

[21]*Dept. of Physics, Durham University, South Road, Durham DH1 3LE, England*

[22]*Max-Planck-Institut für Astrophysik, Karl-Schwarzschild-Str. 1, D-85748 Garching, Germany*

[23]*Physik-Department, Technische Universität München, James-Franck-Straße 1, D-85748 Garching, Germany*

[24]*Institute of Astronomy and Astrophysics, Academia Sinica, PO Box 23-141, Taipei 10617, Taiwan*

[25]*Cerro Tololo Inter-American Observatory, National Optical Astronomy Observatory, Casilla 603, La Serena, Chile*

[26]*CNRS, UMR 7095, Institut d'Astrophysique de Paris, F-75014, Paris, France*

[27]*Sorbonne Universités, UPMC Univ. Paris 06, UMR 7095, Institut d'Astrophysique de Paris, F-75014, Paris, France*

[28]*Department of Physics & Astronomy, University College London, Gower Street, London WC1E 6BT, UK*

[29]*Laboratório Interinstitucional de e-Astronomia – LIneA, Rua Gal. José Cristino 77, Rio de Janeiro, RJ-20921-400, Brazil*

[30]*Observatório Nacional, Rua Gal. José Cristino 77, Rio de Janeiro, RJ-20921-400, Brazil*

[31]*Department of Astronomy, University of Illinois at Urbana-Champaign, 1002 W. Green Street, Urbana, IL 61801, USA*

[32]*National Center for Supercomputing Applications, 1205 West Clark Str, Urbana, IL 61801, USA*

[33]*Institut de Física d'Altes Energies (IFAE), The Barcelona Institute of Science and Technology, Campus UAB, E-08193 Bellaterra (Barcelona), Spain*

[34]*Kavli Institute for Particle Astrophysics and Cosmology, PO Box 2450, Stanford University, Stanford, CA 94305, USA*

[35]*Centro de Investigaciones Energéticas, Medioambientales y Tecnológicas (CIEMAT), Madrid, Spain*

[36]*Department of Physics, IIT Hyderabad, Kandi, Telangana 502285, India*

[37]*Institut d'Estudis Espacials de Catalunya (IEEC), E-08193 Barcelona, Spain*

[38]*Institute of Space Sciences (ICE, CSIC), Campus UAB, Carrer de Can Magrans, s/n, E-08193 Barcelona, Spain*

[39]*Instituto de Fisica Teorica UAM/CSIC, Universidad Autonoma de Madrid, E-28049 Madrid, Spain*

[40]*Department of Astronomy, University of Michigan, Ann Arbor, MI 48109, USA*

[41]*Department of Physics, University of Michigan, Ann Arbor, MI 48109, USA*

[42]*SLAC National Accelerator Laboratory, Menlo Park, CA 94025, USA*

[43]*Department of Physics, ETH Zurich, Wolfgang-Pauli-Strasse 16, CH-8093 Zurich, Switzerland*

[44]*Santa Cruz Institute for Particle Physics, Santa Cruz, CA 95064, USA*

[45]*Max Planck Institute for Extraterrestrial Physics, Giessenbachstrasse, D-85748 Garching, Germany*

[46]*Universitäts-Sternwarte, Fakultät für Physik, Ludwig-Maximilians Universität München, Scheinerstr. 1, D-81679 München, Germany*

[47]*Harvard-Smithsonian Center for Astrophysics, Cambridge, MA 02138, USA*

[48]*Australian Astronomical Observatory, North Ryde, NSW 2113, Australia*

[49]*Departamento de Física Matemática, Instituto de Física, Universidade de São Paulo, CP 66318, São Paulo, SP, 05314-970, Brazil*

[50]*Department of Physics and Astronomy, University of Pennsylvania, Philadelphia, PA 19104, USA*

[51]*George P. and Cynthia Woods Mitchell Institute for Fundamental Physics and Astronomy, and Department of Physics and Astronomy, Texas A&M University, College Station, TX 77843, USA*

[52]*Department of Astrophysical Sciences, Princeton University, Peyton Hall, Princeton, NJ 08544, USA*

[53]*Institució Catalana de Recerca i Estudis Avançats, E-08010 Barcelona, Spain*

[54]*Jet Propulsion Laboratory, California Institute of Technology, 4800 Oak Grove Dr., Pasadena, CA 91109, USA*
[55]*School of Physics and Astronomy, University of Southampton, Southampton SO17 1BJ, UK*
[56]*Brandeis University, Physics Department, 415 South Street, Waltham, MA 02453, USA*

[57]*Instituto de Física Gleb Wataghin, Universidade Estadual de Campinas, 13083-859, Campinas, SP, Brazil*
[58]*Computer Science and Mathematics Division, Oak Ridge National Laboratory, Oak Ridge, TN 37831, USA*

This paper has been typeset from a T_EX/L^AT_EX file prepared by the author.